Combined effects of temperature and of high hydrogen and oxygen contents on the mechanical behavior of a zirconium alloy upon cooling from the βZr phase temperature range

Thai Le Hong, Jean-Christophe Brachet, Jérôme Crépin, Matthieu Le Saux

Combined effects of temperature and of high hydrogen and oxygen contents on the mechanical behavior of a zirconium alloy upon cooling from the β_{Zr} phase temperature range

Thai Le Hong [a, b], Jean-Christophe Brachet [a*], Jérôme Crépin [b], Matthieu Le Saux [a, c]

[a] *DES-Service de Recherches Métallurgiques Appliquées (SRMA), CEA, Université Paris-Saclay, F-91191 Gif-sur-Yvette, France*
[b] *MINES ParisTech, PSL Research University, Centre des Matériaux, CNRS UMR 7633, BP 87, 91003 Evry, France*
[c] *Now at ENSTA Bretagne, UMR CNRS 6027, IRDL, F-29200 Brest, France*

Abstract

During hypothetical loss-of-coolant accidents (LOCA), zirconium-based nuclear fuel claddings can be exposed to high temperatures in the β_{Zr} phase domain and absorb substantial amounts of hydrogen (up to about 3000 weight ppm) and oxygen (up to about 1 weight %). This paper provides novel data about the combined effects of high hydrogen and oxygen contents on the mechanical behavior of the (prior-)β_{Zr} phase, as a function of temperature, upon cooling from the β_{Zr} phase temperature range. A protocol was developed to homogeneously charge Zircaloy-4 cladding tubes at different hydrogen contents, up to 3200 weight ppm, and oxygen contents, between 0.13 and 0.9 weight %. Tensile tests were then performed at various temperatures between 700 and 30°C upon cooling from the β_{Zr} domain. The results show that the mechanical behavior strongly depends on the testing temperature and the hydrogen and oxygen contents. Relationships are proposed to describe the macroscopic ductile-to-brittle transition and the mechanical behavior of the material as a function of temperature, hydrogen and oxygen contents. The predictions based on these relationships are compared to selected data from the literature obtained on claddings oxidized at high temperature, including results from semi-integral LOCA tests. Also, it is shown that considering the combined effects of hydrogen and oxygen is necessary to interpret the material's mechanical behavior, particularly the embrittlement of claddings subjected to LOCA-relevant secondary hydriding.

Keywords: Zircaloy-4, LOCA, secondary hydriding, hydrogen, oxygen, mechanical behavior, high temperature.

1 Introduction

During a hypothetical loss-of-coolant accident (LOCA) in light water reactors, the fuel cladding made of zirconium alloys can be subjected to internal pressure and exposed to steam at high temperature (HT), between 700 and 1200°C typically, before being cooled at a rate of about 1-10°C/s down to 500-800°C, then water-quenched by the emergency core cooling system [1]. Internal pressure can lead to ballooning and burst of the cladding due to a decrease in the system pressure outside the fuel rod and the degradation of cladding strength [2,3]. During heating, the low-temperature hexagonal

* Corresponding author.
Email address: jean-christophe.brachet@cea.fr (J.C. Brachet)

close-packed α_{Zr} phase transforms into the HT body-centered cubic β_{Zr} phase [4]. A significant fraction of the oxygen resulting from the oxidation reaction by steam at HT diffuses into the metal. Once the oxygen solubility limit is reached in the β_{Zr} phase, a metallic layer of oxygen-stabilized α_{Zr} phase, called α_{Zr}(O), forms between the oxide and the β_{Zr} phase layers. During cooling, the β_{Zr} phase transforms back to the α_{Zr} phase and forms the so-called prior-β_{Zr} structure with the typical Widmanstätten structure that can be easily distinguished from the equiaxed α_{Zr}(O) structure [5,6]. Also, at the end of the LOCA transient, the cladding is subjected to thermally-induced internal stresses associated with additional axial tensile loading, which may cause failure [7–9]. In accordance with the safety requirements, it is essential that the cladding retains some mechanical resistance or ductility to ensure its integrity and a coolable core geometry during and after a LOCA transient. At the end of a LOCA transient, the cladding's mechanical strength and ductility mainly result from the mechanical properties of the residual prior-β_{Zr} phase layer [6,10–12]. It was found that the mechanical behavior of this layer is strongly influenced by its oxygen and hydrogen contents [6,11,13,14].

In order to investigate the behavior of fuel claddings during the LOCA scenarios, a large number of so-called "semi-integral" LOCA tests have been performed not only with single unirradiated or irradiated fuel rods [2,7,9,15,16] but also with a bundle of rods [17,18]. Such tests reproduce the full effects of a LOCA transient on the cladding: heating, ballooning and burst, HT oxidation in steam followed by cooling and water-quenching with or without an additional tensile load. The results have shown a fast and substantial secondary hydriding of the cladding after only a-few-tens-of-seconds exposure to steam at HT [2]. Secondary hydriding consists of massive hydrogen uptake, up to thousands of weight ppm (wppm) locally, observed at a few centimeters away from the burst opening. The results of these semi-integral LOCA tests showed that, depending in particular on the HT oxidation and mechanical loading conditions, cladding fracture during reflooding can occur (i) in the burst region where the oxidation level is the highest, (ii) in the secondary hydrided region where the hydrogen content is the largest, or (iii) between these two zones, where the hydrogen content and the oxidation level are high but not maximal. Then, the cladding's failure during quenching and its location (when it exists) are often related to the residual thickness of the β_{Zr} layer and the "local" hydrogen content [7,9]. Besides, apart from the structure effects, *i.e.* β_{Zr} layer thinning due to steam oxidation associated with oxygen diffusion at HT, the post-secondary hydriding embrittlement of the cladding is often exclusively related to the high hydrogen contents in the secondary hydrided regions [7,9]. However, the oxygen content in the β_{Zr} layer is also expected to play a role. Thus, it should be taken into account to interpret more accurately the results of the semi-integral LOCA tests, especially when investigating the hydrogen-induced embrittlement mechanisms in the secondary hydrided regions [19,20]. Indeed, recent results [19] have shown that the larger the hydrogen concentration in the β_{Zr} phase in the secondary hydrided regions, the higher the oxygen content. Precisely, after oxidation at 1100 and 1200°C, high oxygen contents, attaining up to 1-1.2 weight % (wt%), equivalent to about 5 atomic % (at%), were measured in the β_{Zr} phase in the presence of high hydrogen contents, up to about 3000-4000 wppm, or 20-25 at% [19]. It is important to note that the solubility limit of oxygen in the β_{Zr} phase at 1100-1200°C is lower than 0.5-0.6 wt% in the absence of hydrogen [6,21,22]. This correlation between hydrogen and oxygen contents in the β_{Zr} phase in the secondary hydrided regions can be essentially related to

hydrogen's thermodynamic effect on oxygen solubility and diffusivity in this phase at HT [2,13,21,23–25].

So far, the majority of data about the mechanical properties of the (prior-)β_{Zr} phase were obtained on materials enriched either in hydrogen or in oxygen. Furthermore, they often concern hydrogen and oxygen contents lower than the high contents of interest here. In addition, these data were mostly obtained at low temperatures, 20 and 135°C, typically. However, it is obvious that temperature significantly affects the mechanical behavior of the (prior-)β_{Zr} material and the respective effects of oxygen and hydrogen [6,10,11]. A few data also suggested that oxygen and hydrogen have combined effects on the mechanical properties of the (prior-)β_{Zr} phase [19].

The present work is devoted to thoroughly studying the mechanical behavior of the (prior-)β_{Zr} phase containing both hydrogen and oxygen with high contents as a function of temperature upon cooling from the β_{Zr} domain. The first section of the present paper describes the material and experimental procedures. A protocol was developed to produce, from Zircaloy-4 cladding tubes, "model" prior-β_{Zr} phase materials homogeneously charged with hydrogen and oxygen at different contents: 1000-3000 wppm of hydrogen and 0.5-0.9 wt% of oxygen. These contents are in the same order of magnitude as those likely to be encountered in the (prior-)β_{Zr} layer of claddings oxidized at HT under steam and having experienced LOCA-relevant secondary hydriding. Note that this step required many optimization works. To our knowledge, this is the first time that prior-β_{Zr} phase materials containing such high contents of both hydrogen and oxygen were fabricated from cladding tubes in a controlled manner. The procedure used to characterize the mechanical behavior of these model materials upon cooling from HT is then presented. The tests were performed between 700°C and room temperature (RT). 700°C is the typical temperature before final quenching upon semi-integral lOCA transients. The experimental results obtained are presented in Section 3. In Section 4, these data are used to determine relationships describing the evolutions of the macroscopic ductile-to-brittle transition and the mechanical properties as a function of hydrogen and oxygen contents and temperature. Finally, the results are discussed and compared with selected data from the literature in Section 5, including those from semi-integral LOCA tests.

2 Materials and experimental procedures

2.1 Sample preparation

The samples were prepared from stress-relieved annealed low-tin Zircaloy-4 fuel cladding tubes with a typical chemical composition of 1.3 wt% Sn, 0.2 wt% Fe, 0.1 wt% Cr, 0.13 wt% O, less than 5 wppm H, Zr balance. Their outer diameter and wall thickness were 9.5 mm and 0.57 mm, respectively. Tube samples were homogeneously charged at different hydrogen contents, from about 1000 to 3000 wppm (about 10-20 at%), and different oxygen contents, between approximately 0.5 and 0.9 wt% (2-5 at%). The preparation protocol consists of three main steps: hydrogen charging, oxygen charging, and homogenization, which are detailed in the following.

2.1.1 Hydrogen charging

As-received Zircaloy-4 66 mm-long cladding tube segments were first charged with hydrogen at different contents, from about 1000 to 3000 wppm. The hydrogen charging was conducted at 800°C in a flowing argon/hydrogen gas mixture using a protocol based on that developed in [11] and [26]. The hydrogen partial pressure was chosen as approximatively 5.2-5.5x10^3 Pa with the exposure duration to argon/hydrogen flow at 800°C depending on the desired hydrogen content [26]. To fully homogenize the hydrogen concentration, the samples were then heat-treated at 800°C for about one hour under nearly pure argon gas, then slowly cooled at a few °C/min down to RT.

The hydrogen contents were systematically measured on all the samples after hydrogen charging using an inert gas fusion thermal conductivity technique (HORIBA EMGA-821 analyzer). The hydrogen content measurements were conducted on three to seven 2 mm-long rings sectioned at different locations on the 66 mm-long tubes to check axial homogeneity. Each ring was then divided into three parts so that three measurements were performed to verify the hydrogen concentration's azimuthal homogeneity.

2.1.2 Oxygen charging

After hydrogen charging, some samples were charged with oxygen at contents between about 0.5 and 0.9 wt%, using a two-steps protocol based on the one used in [6,10,11] to charge non-hydrided materials with oxygen. First, the samples were cut into two 30 mm-long segments that were then oxidized (two-sided oxidation) under flowing steam at 1000°C in the facility called DEZIROX 2 [28]. The oxidation times were determined on the basis of the target amount of oxygen using the available oxidation kinetics established in prior studies [29]. At the end of steam oxidation, the samples were directly dropped into RT water. The weight gain due to oxidation was then calculated from the sample mass measured before and after oxidation, providing the average amount of oxygen absorbed, hereafter referred to as the oxygen content deduced from the weight gain.

Metallographic examinations have shown that the oxide layer thickness is homogeneous along the samples as well as between inner and outer sample surfaces. Hydrogen content measurements carried out on some samples after oxidation have not revealed significant hydrogen pick-up, a few tens of wppm at most. This indicates that the oxidation times applied were shorter than those inducing significant hydrogen uptake at 1000°C, *i.e.* for post-breakaway oxidation [30].

2.1.3 HT homogenization

After hydrogen charging and steam oxidation at 1000°C, the samples were heat-treated at 1200-1300°C under inert gas to homogenize oxygen by reducing the oxide layer's thickness by oxygen diffusion across the sample thickness. For this purpose, a protocol based on a procedure successfully applied to hydrogen-free sheet samples [31] was developed and optimized in our study. It can be summarized as follows:

- The samples were first encapsulated in quartz bulbs to prevent air oxidation at HT. The free volume inside the bulb has been reduced as much as possible in order to limit hydrogen desorption during the homogenization heat-treatment. Thus, 3-4 30 mm-long tube samples containing the same average hydrogen and oxygen contents were inserted into a quartz tube with 10 mm of internal diameter and 12-15 cm of length. A 7-8 mm-diameter full cylindrical quartz rod was then placed inside the remaining free volume.
- Before sealing the quartz bulbs, a primary vacuum was applied to remove the residual air. A certain amount of argon (99.997 volume %) was then injected into the bulbs with a gas pressure depending on the hydrogen content: 100 mbar for hydrogen contents below 1000 wppm, 50 mbar for 1500-2000 wppm of hydrogen, and 20 mbar for hydrogen contents around 3000 wppm. The gas pressures were chosen to prevent the bulbs from contraction, ballooning, or even burst, but also to limit hydrogen desorption during the heat-treatment at 1200-1300°C (related to the evolution of the hydrogen partial pressure according to Sieverts' law [32]).
- The quartz bulbs were then heat-treated at 1200-1300°C for four hours in a furnace. The annealing temperatures were limited to 1300°C as to avoid damage to the quartz tubes used. The heat-treatment temperatures were chosen considering that temperature had to be sufficiently high to fully transform the material into the β_{Zr} phase, but not too high to limit hydrogen desorption at HT. The treatments were finally performed at 1300°C for samples containing less than 1000 wppm of hydrogen and at 1200°C for those containing more hydrogen. At the end of the heat-treatments, the bulbs were rapidly taken out of the furnace, then broken in RT water to obtain a water-quenched microstructure. The samples containing less than 1000 wppm of hydrogen were directly quenched in RT water. The samples charged with 2000-3000 wppm hydrogen were cooled at 1-3°C/s down to 1100°C before water quenching with the aim to allow the samples to reabsorb some of the hydrogen that may have desorbed during the treatment at 1200°C. No sample failed during water-quenching, allowing further mechanical characterizations.

2.1.4 Oxygen and hydrogen contents measurements

After HT homogenization, the samples' microstructure, the average oxygen and hydrogen contents, and their homogeneity, were systematically characterized (in addition to the analyses made after each step of the model material preparation protocol).

Hydrogen content

The hydrogen content measurements performed after homogenization using the HORIBA EMGA-821 analyzer show nearly no hydrogen desorption during the heat-treatments. There may have been some hydrogen losses (for example during the one hour annealing at 800°C under nearly pure argon, according to the Sieverts' law [27]) but in amounts too small, *i.e.* smaller than the uncertainties resulting from hydrogen charging and hydrogen content measurement (considering that the hydrogen contents studied here are very high), to be clearly observed.

In order to check the axial homogeneity of the hydrogen concentration, hydrogen content measurements were performed at three different positions of some tube samples (at the two ends and in the middle) using the HORIBA EMGA-821 analyzer. Besides, a non-destructive analysis using neutron radiography was carried out at the Léon Brillouin laboratory (LLB, CEA, CNRS, Université Paris-Saclay, France) on a 35 mm-long tube sample containing, on average, 2600-2700 wppm of hydrogen and 0.4 wt% of oxygen (content deduced from the weight gain), heat-treated at 1200°C. Samples with known hydrogen contents (previously measured by HORIBA EMGA-821 analyzer) in the range investigated were used as reference samples for hydrogen content calibration [19,33]. Note that hydrogen plays a major role in neutron absorption and the contribution of oxygen can be neglected. As shown in Fig. **1**, the variation is only ±10% in hydrogen concentration along the sample's whole length. The azimuthal variation in the hydrogen content is only a few wppm to a few tens of wppm.

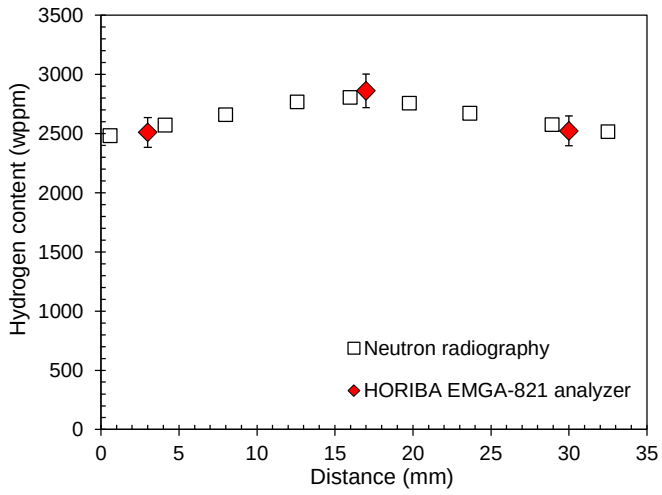

Fig. 1. Hydrogen contents measured on a Zircaloy-4 tube sample containing 2600-2700 wppm of hydrogen and 0.4 wt% of oxygen on average, heat-treated at 1200°C, using the HORIBA EMGA-821 analyzer and neutron radiography.

Oxygen content

An example of the microstructure of a sample charged with hydrogen and oxygen after homogenization heat-treatment is illustrated in Fig. **2**. It is shown that the microstructure exhibits a 100% prior-β_{Zr} structure with neither residual oxide layer nor oxygen-enriched α_{Zr}(O) layer.

In order to indirectly check the homogeneity (at the macroscopic scale) of the oxygen content, which is known to have a significant hardening effect on prior-β_{Zr} [13], microhardness measurements were carried out across the sample thickness using a Vickers diamond indenter with a load of 100g. The microhardness profiles made an angle of 45° from the tube radial direction, with a distance of 50 µm between indentation marks. As shown in Fig. **2**(a), the oxygen distribution in the samples is macroscopically uniform after HT homogenization. Slight variations in the microhardness values can be observed, related to oxygen redistribution resulting from

the β_{Zr}-to-α_{Zr} phase transformation during cooling, leading to the formation of oxygen-enriched and oxygen-depleted zones at the microstructure scale [6,24]. In the case of materials charged with both hydrogen and oxygen, it is found that hydrogen has no significant effect on the Vickers microhardness values and that only the effect of oxygen can be pointed out. This observation is consistent with the result given in [19]. This confirms that for the water-quenched prior-β_{Zr} structure, the hardening effect of oxygen is significantly more important than that of hydrogen.

Infrared absorption analyses (LECO TC500 analyzer) performed on samples only charged with hydrogen showed slight oxygen uptake (about 0.1 wt%) during hydrogen charging, so these samples contain approximately 0.2-0.3 wt% of oxygen on average.

The hydrogen contents in the samples can be approximatively divided into four principal ranges: 20-30, ~1000, ~2000, and ~3000 wppm; completed with three sets of oxygen contents: ~0.2, ~0.5, and ~0.9 wt%. These contents cover most of the content ranges encountered in the prior-β_{Zr} layer within fuel claddings that have experienced (semi-)integral LOCA transients with secondary hydriding.

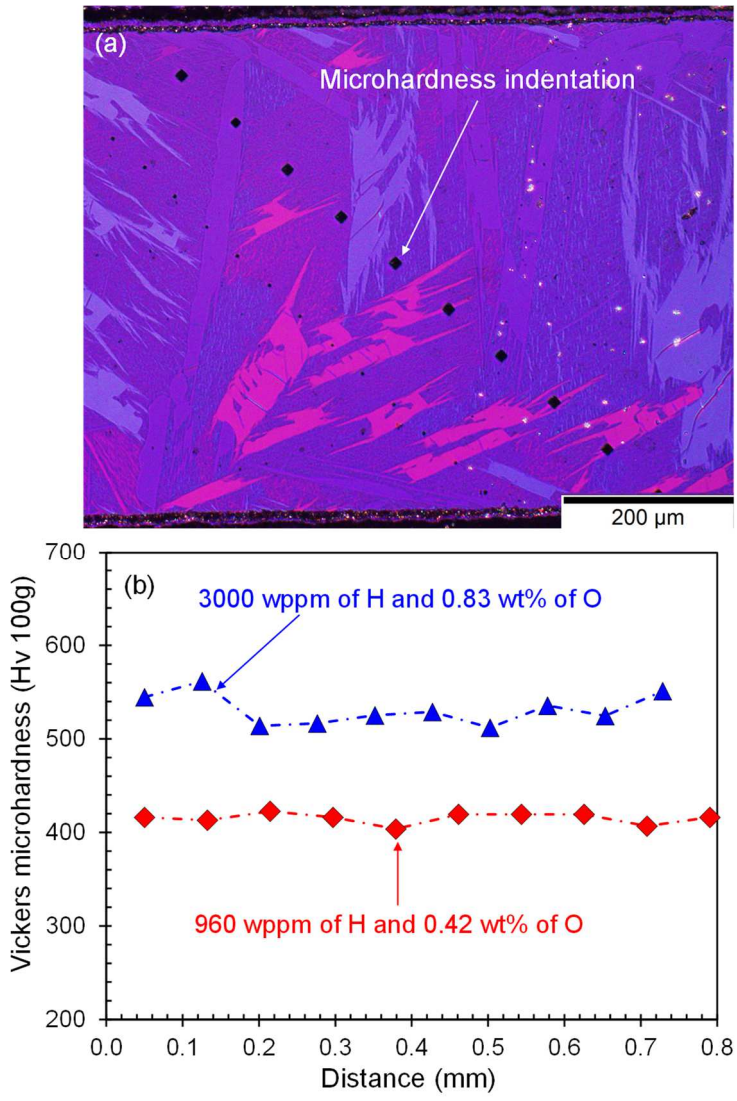

Fig. 2. (a) Polarized optical micrograph of the transverse cross-section of a sample containing 3000 wppm hydrogen and 0.83 wt% oxygen, (b) Vickers microhardness values measured after homogenization heat-treatments at 1200-1300°C across the thickness of samples charged with hydrogen and oxygen.

2.2 Mechanical testing

2.2.1 Specimen preparation

In order to characterize the macroscopic mechanical behavior of the model materials upon cooling from the β_{Zr} domain, uniaxial tensile tests were performed on specimens, with 8 mm of gauge length and 2 mm of gauge width, fabricated from Zircaloy-4 cladding tube segments homogeneously charged with hydrogen, at a few wppm to 3200 wppm, and with oxygen, at 0.13-0.84 wt%. The specimen geometry, already used in [11], is illustrated in Fig. **3**. The tensile specimens were machined by electro-erosion (tungsten wire). This technique helps minimize the force applied to the samples during machining, which could lead to the failure of samples highly enriched in hydrogen and oxygen, likely to be very brittle at low temperature. Despite the precautions taken beforehand, many specimens were broken during preparation, especially those containing both high hydrogen contents and high oxygen contents, ~2000-3000 wppm hydrogen and ~0.9 wt% oxygen typically.

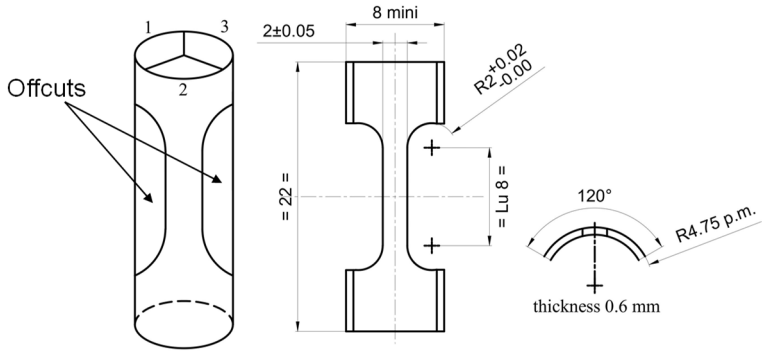

Fig. 3. Tensile specimen geometry.

In addition to the characterizations mentioned in Section 2.1.4, for each specimen, average hydrogen and oxygen content measurements were systematically performed on 130-150 mg offcuts resulting from the specimen machining. The oxygen contents of the specimens were estimated from:

- the weight gain measured after steam oxidation at 1000°C and prior to HT homogenization;
- 100g Vickers microhardness measurements performed across the prior-β_{Zr} layer thickness of some machining offcuts after HT homogenization using the correlations proposed by Brachet *et al*. [13] relating the oxygen content to the microhardness value for the water-quenched prior-β_{Zr} structure (this relationship may tend to slightly overestimate the oxygen content in the presence of high hydrogen contents);
- Electron Probe Microanalyses (EPMA) performed on some machining offcuts after HT homogenization, with oxygen profiles measured across the whole prior-β_{Zr} layer thickness, parallel to and near the microhardness profiles.

It has been found that the oxygen contents deduced from the weight gains are in good agreement with those estimated from microhardness and EPMA. As a result, it is assumed that there was no significant oxygen uptake during the HT homogenization treatments. The oxygen contents mentioned hereafter for each specimen are deduced from the weight gain measurements.

2.2.2 Experimental procedures

The tensile tests were carried out on a MTS servo-hydraulic tensile testing system equipped with a 2.5 kN load cell, using the same experimental procedures presented in [11,26]. During the tests, the specimen holder's temperature was directly monitored using two Chromel-Alumel thermocouples spot-welded on its upper and lower regions, and another welded next to the specimen, providing the so-called "furnace" temperature. Because of the specimen's small size and fragility, it was not possible to directly weld thermocouples on it. Consequently, it was necessary to carry out calibration tests to estimate the specimen's temperature from the furnace temperature during a typical thermal cycle applied before and during the tensile tests (the specimens were heat-treated in the β_{Zr} domain and mechanically tested upon cooling), as illustrated in Fig. **4**.

Due to the potential fragility of the specimens and the HT reached during the tensile tests, it was not possible to utilize an extensometer to measure the displacement of the specimen gauge region directly. Therefore, the displacement fields in the specimen gauge region were determined by two-dimensional (2D) digital image correlation (DIC). In order to obtain sufficient optical contrast for image correlation, the gauge surface of each specimen was painted beforehand with a random pattern consisting of points made of a titanium dioxide-based white fluid using an airbrush. The white titanium dioxide was chosen since it exhibits good HT resistance and good contrast with the dark specimen surface. A rectangular window was made on one side of the furnace, through which images of the specimen surface were taken using a fast Photron camera (Fastcam SA1.1) at a rate of 250 images per second. The specimen surface was illuminated in white light using two LED lamps

2.2.3 Testing conditions

The tensile tests were conducted at various temperatures between 700 and 30°C upon cooling from 1000-1200°C in the β_{Zr} domain: 700, 580, 500, 400, 350, 135, and 30°C. The tests were performed in the air so that a thin oxide layer of about 3-5 μm of thickness was formed on the specimen surfaces. It has been believed that the thin zirconia layer formed *in situ* may help avoid hydrogen desorption at HT. Along with this, a certain quantity of oxygen diffuses into the metal, leading to the formation of a thin α_{Zr}(O) layer of about 3-7 μm of thickness beneath the oxide layer, but no significant oxygen enrichment in the β_{Zr} layer. Besides, no zirconium nitride was observed after testing. The white titanium dioxide points used for DIC remained visible after the heat-treatment at HT.

As shown in Fig. **4**, after being mounted on the testing machine, the specimen was rapidly heated up to the β_{Zr} domain at 1000-1200°C, at about 8-10°C/s up to 1000°C then 4°C/s between 1000-1200°C on average. Maximum temperatures of 1000°C and 1150-1200°C were applied to the specimens only charged with hydrogen and to those charged with both hydrogen and oxygen, respectively. On the one hand, the temperature needs to be high enough to transform the materials into the β_{Zr} phase. The choice was made on the basis of thermodynamic predictions at equilibrium, obtained by the Thermo-Calc software associated with the Zircobase database [32,34]. However, under the dynamic conditions of the tests performed, the temperatures above which the material is entirely in the β_{Zr} phase are certainly higher than those predicted at equilibrium. On the other hand, the temperature chosen should not be too high to limit air oxidation and oxygen diffusion from the external specimen surfaces into the underlying metallic layer. Once the maximum temperature was attained, the furnace was immediately turned off so that the specimen was directly cooled down to the target temperature for the tensile test that was then launched without delay. The specimen cooling rate was higher than 5-6°C/s between the beginning of cooling and 700°C, then ~1-2°C/s from 700 to 500°C, and lower than 1°C/s for temperatures below. These relatively rapid cooling rates are of the same order of magnitude as those expected during a LOCA transient before the final water-quenching from 500-800°C [1].

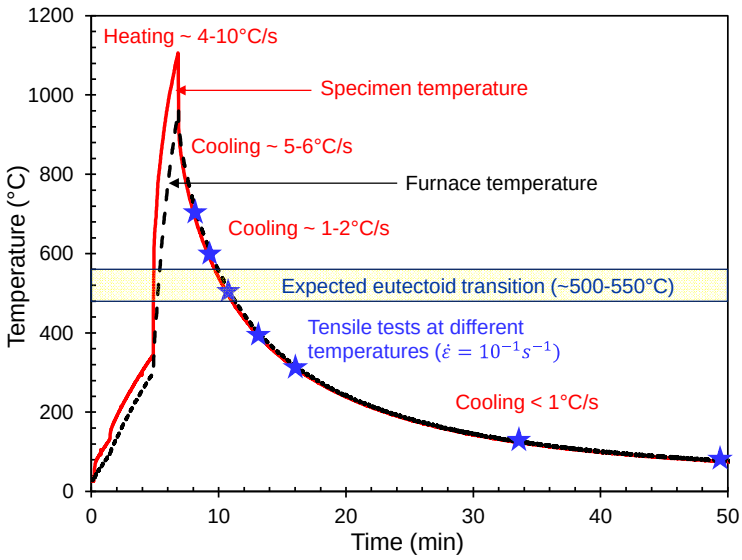

Fig. 4. Typical thermal cycle applied during the tensile tests: evolution of the temperature measured on the specimen holder (furnace temperature) and the specimen surface (specimen temperature); the blue stars denote the temperatures at which the tensile tests were performed.

The tests were performed under displacement control, including during the thermal cycle (tests had been carried out with a force control during the thermal cycle to compensate for the thermal expansion effects, but the control was not satisfactory). To limit the stresses during the thermal cycle before the tensile test, a gap was initially left between the moving holder and the specimen, allowing the specimen to expand freely. The specimens were subjected to a maximum compressive stress of approximately 4-5 MPa during the thermal cycle, *i.e.* in the elastic range of the material. The tests were performed at a constant crosshead displacement rate of 0.8 $mm \cdot s^{-1}$, equivalent to an approximate mean strain rate of 0.1 s^{-1} in the specimen gauge region. This relatively

rapid strain rate, leading to testing durations of 1-2 s typically, made it possible to limit both oxidation and metallurgical evolutions of the materials during the tests, as well as temperature variations. It was estimated that the specimen temperature variation during the test and the temperature gradient along the specimen gauge length do not exceed 10°C. Besides, the strain rate applied is expected to be faster than that commonly used in semi-integral LOCA tests, based on the rough estimates made from the data reported in [7,35]. The mechanical behavior of the material probably depends on the loading rate. However, this effect is expected to be second-order compared to the combined effects of temperature, hydrogen, and oxygen.

2.2.4 Data analysis

The tensile load, crosshead displacement, and furnace temperature were routinely recorded throughout the tests. The digital image correlation (local approach) was performed on a 1.5-1.8x8 mm^2 zone called the region of interest (ROI), using the VIC-2D™ software. The Green-Lagrange strains were calculated from the displacement fields. Axial and hoop strains were then averaged over the whole analyzed surface. The uncertainty on the mean strains determined has been estimated at approximately ±0.0004 at best.

The engineering axial stress was defined as the ratio of the force measured by the load cell to the specimen's initial cross-section in the gauge region. The maximum axial strain determined by DIC was limited to a few % because of the pattern's cracking (embrittled after the HT treatment) for larger strain levels. As a consequence, the engineering axial strain was deduced from the DIC for the elastic domain and the beginning of plasticity, up to 0.03 % of plastic strain. For higher axial strain levels, the axial strain was estimated by dividing the crosshead displacement by the specimen gauge length. In this case, the plastic part (supposed to be fully related to the specimen) of the strain determined from the crosshead displacement was isolated by removing the elastic part of the strain determined from the crosshead displacement using the initial slope of the stress-strain curve (with the strain obtained from the crosshead displacement). The total strain was then obtained by adding this plastic strain to the elastic strain calculated from the stress using Young's modulus determined from the stress-strain curve with the strain obtained by DIC.

The following mechanical parameters were determined from the engineering stress-strain curves: Young's (elastic) modulus (E), yield stress at 0.2% offset (YS), ultimate tensile strength (UTS) consisting of the maximum stress that the material can withstand during the tensile test, uniform elongation (UE, plastic strain at the maximum stress, corresponding to the plastic strain at the onset of necking in the case of existence), and plastic strain at failure (PSF). Besides the plastic strain at failure, the reduction of cross-section area at fracture (Z) was measured from optical images taken perpendicularly to the tensile direction on both sample's fracture surfaces to characterize the ductility of the material. It has been estimated that the absolute uncertainty of these measurements is about ±0.08. UE, PSF and Z are null as the specimen fails in the elastic domain (brittle failure). Tabular data from the tensile tests are given in Appendix.

3 Experimental results

3.1 Stress-strain response

Fig. **5** gives examples of engineering stress-strain curves obtained for specimens charged with hydrogen and oxygen at different contents, tested at various temperatures between 700 and 30°C upon cooling from the β_{Zr} domain. It is shown that the mechanical response strongly depends on temperature and hydrogen and oxygen contents.

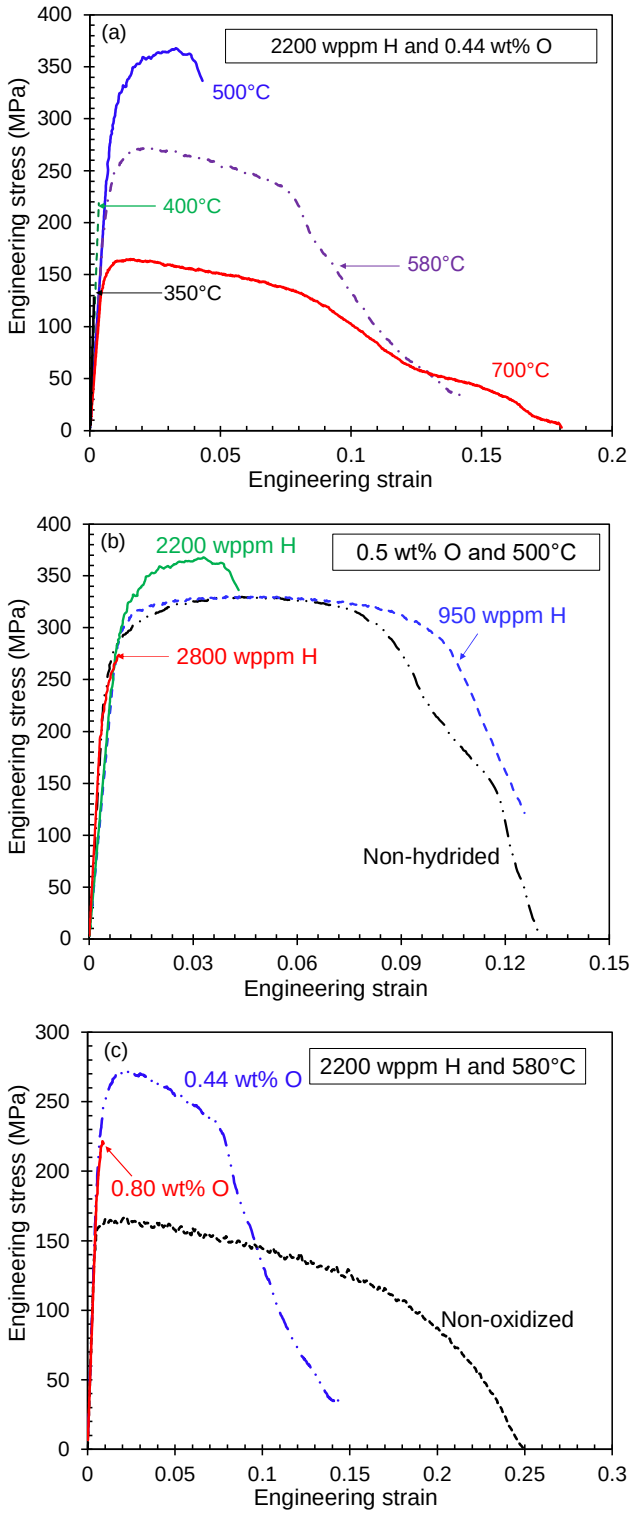

Fig. 5. Engineering stress-strain curves for Zircaloy-4 charged at different hydrogen and oxygen contents, tested in tension at various temperatures between 700 and 30°C upon cooling from the β_{Zr} phase domain.

3.2 Elastic modulus

Fig. **6** shows the temperature dependence of E. As mentioned earlier, thin ZrO_2 and $\alpha_{Zr}(O)$ layers formed on the specimen surfaces due to air oxidation during the tensile

tests. These phases, which are likely not to be cracked at the beginning of the tensile tests, have elastic moduli significantly higher than that of the (prior-)β_{Zr} phase less enriched in oxygen [6,12,36]. However, given their relatively small thickness compared to the whole thickness of the specimen, it is reasonable to assume that their contribution to the elastic modulus value is included in measurement uncertainty.

As can be observed in Fig. **6**, the elastic moduli of the materials increase continuously as temperature decreases between 700 and 30°C, regardless of hydrogen and oxygen contents. However, given scattered data, neither hydrogen nor oxygen in the content ranges studied, *i.e.* up to 3200 wppm of hydrogen and 0.84 wt% of oxygen, has significant effects on the elastic modulus. This is consistent with results from the literature for prior-β_{Zr} only charged with hydrogen, up to 3000 wppm, or with oxygen, up to about 1 wt% [6,11,36].

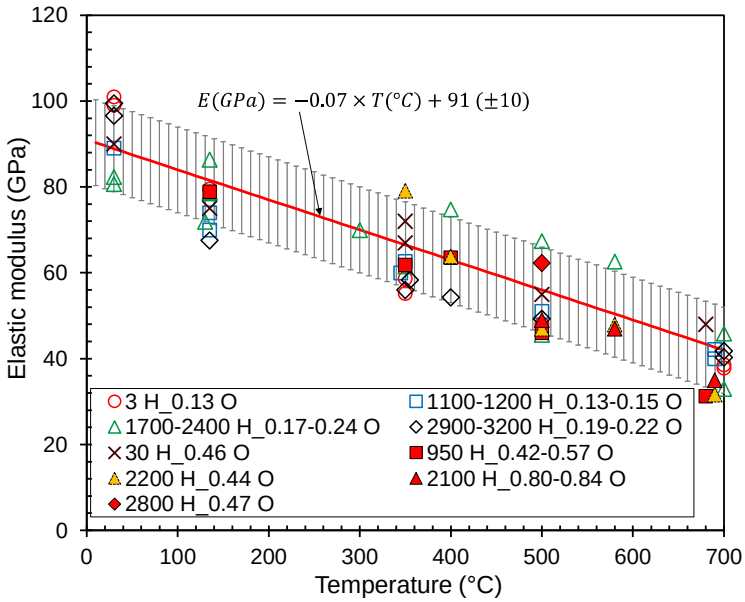

Fig. 6. Temperature dependence of E of the (prior-)β_{Zr} material charged at different hydrogen (in wppm) and oxygen (in wt%) contents; data for materials only charged with 1700-3200 wppm hydrogen are from [11].

3.3 Fracture and ductile-to-brittle transition

Fig. **7** clearly shows a significant decrease in PFS upon cooling between 700 and 30°C, whatever the hydrogen and oxygen contents. It is noticed that all the specimens with the hydrogen and oxygen contents in the ranges studied are ductile at 700°C, with PFS values greater than 0.08. Contrary to the materials only charged with hydrogen, for which the hydrogen-related effect on material ductility is negligible at temperatures above 500°C [11], it is found that in the presence of oxygen, hydrogen reduces the ductility of the material considerably, as illustrated in Fig. **7**(a). It can be seen that there exists a so-called “critical” temperature below which the materials become macroscopically brittle for a given couple of hydrogen and oxygen contents. This temperature is considered as the macroscopic ductile-to-brittle transition (DBT) temperature of the material. This temperature increases with the hydrogen and oxygen contents. The results indicate that the hydrogen-induced embrittlement is intensified

when the material is also charged with oxygen, and *vice versa*. These observations are in good agreement with those based on Z presented in Fig. **8**. Note that a slightly negative Z is obtained for some brittle specimens due to the measurement uncertainty.

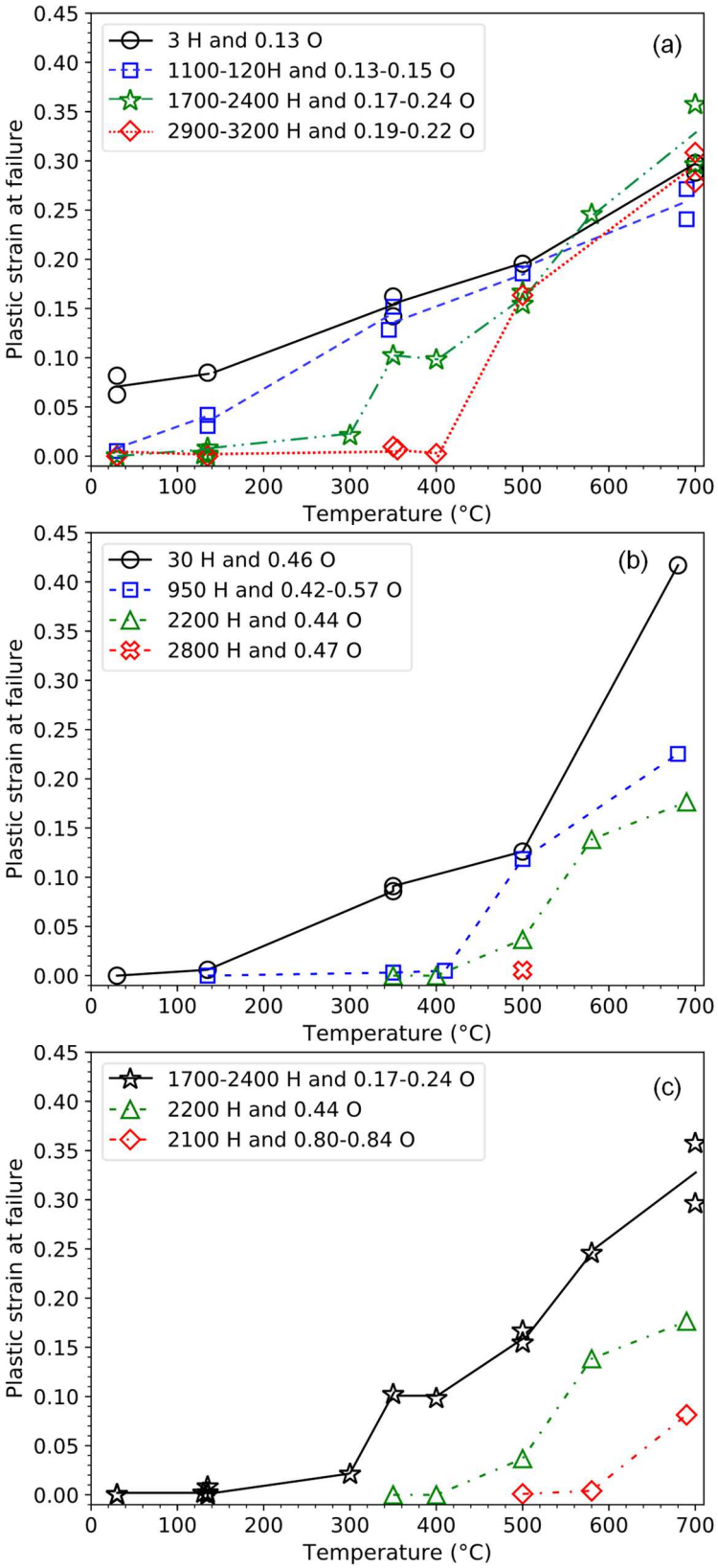

Fig. 7. Temperature dependence of the global PFS of the (prior-)β_{Zr} material containing: (a) ~0.2 wt% oxygen and different hydrogen contents (in wppm), (b) ~0.5 wt% oxygen and different hydrogen contents (in wppm), (c) ~2000 wppm hydrogen and different oxygen contents (in wt%); data on materials only charged with 1700-3200 wppm hydrogen are from [11].

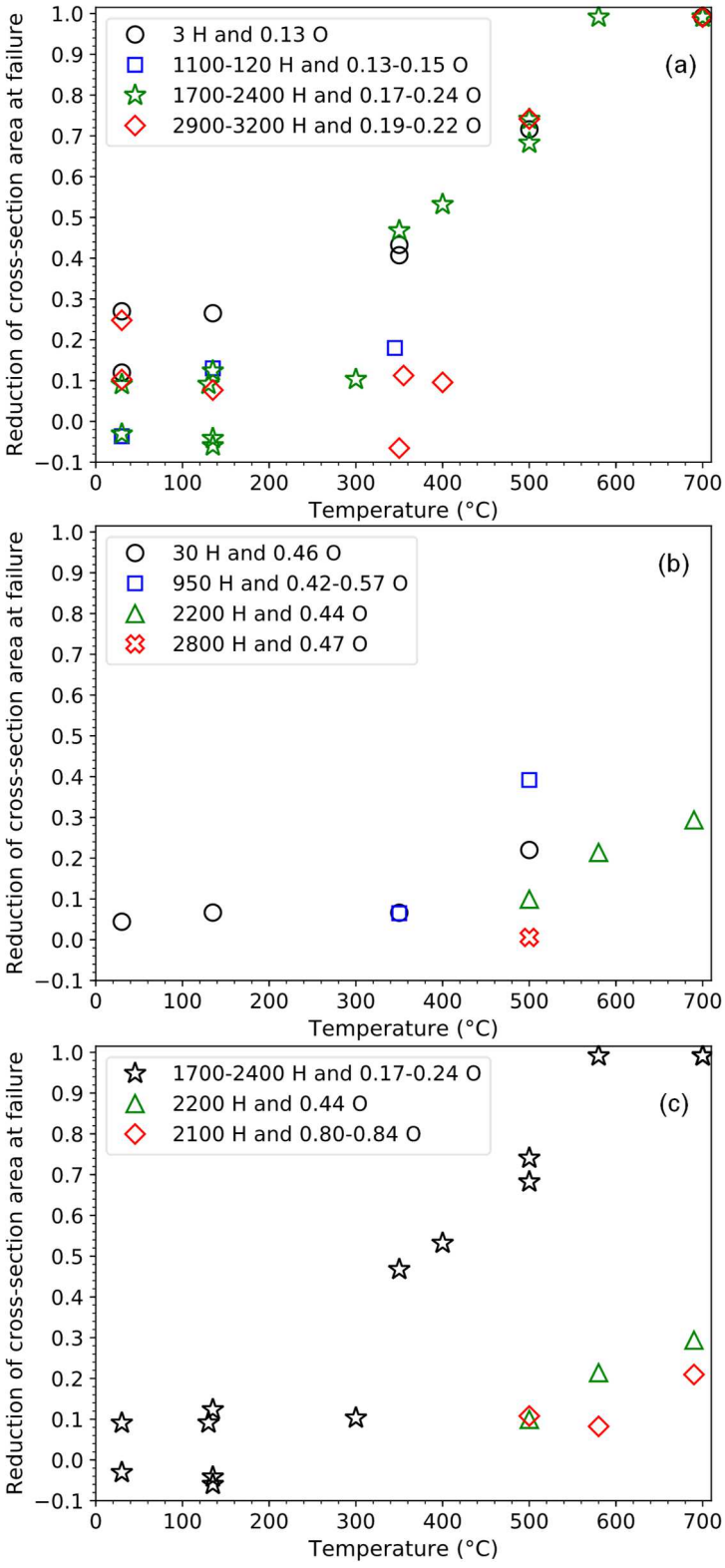

Fig. 8. Temperature dependence of Z of the (prior-)β_{Zr} material containing: (a) ~0.2 wt% oxygen and different hydrogen contents (in wppm), (b) ~0.5 wt% oxygen and different hydrogen contents (in wppm), (c) ~2000 wppm hydrogen and different oxygen contents (in wt%); data on materials only charged with 1700-3200 wppm hydrogen are from [11].

The macroscopic failure mode transition is delimited as follows: the materials are classified as ductile, nearly brittle, and brittle if the plastic strain at failure is higher than 0.01, between 0.01 and 0.005, and below 0.005, respectively. The plastic strain at failure is used rather than the reduction of cross-section area at fracture to establish the macroscopic DBT since the latter's measurements exhibit a considerably higher uncertainty. However, this would not change the trends and conclusions based on the plastic strain at failure.

The macroscopic failure modes determined from our results and data available from the literature [6,12,13,37–40] for materials either charged with hydrogen or oxygen are shown in Fig. **9** and Fig. **10**.

In the case of materials only charged with hydrogen, it can be seen from Fig. **9** that our results are, on the whole, in good agreement with those reported by Bai [38] for Zircaloy-4 flat specimens containing up to 3200 wppm of hydrogen, tested in tension at different temperatures between 20 and 350°C after hydrogen charging at 700°C and cooling at a rate lower than 0.02°C/s. Pshenichnikov *et al.* [37] observed, after cooling at 5°C/s from 727-927°C, macroscopically ductile failure at RT for very high hydrogen contents up to 3400 wppm and a DBT at RT for the material charged with 4850 wppm hydrogen at 927°C. This result appears to be different from ours, which indicate a DBT at RT for about 1000 wppm hydrogen, and from the observations reported by Brachet *et al*. [13], who showed nearly-brittle failure at RT on the material charged with 600-700 wppm hydrogen and directly quenched into water from 1000°C. This difference in the failure mode would be related to the oxygen content in the hydrogen-charged materials tested in our study, which is higher by about 0.1 wt%. This additional oxygen is likely to have a significant effect on the embrittlement of the material. Besides, the faster cooling rate applied by Brachet *et al*. [13] probably induces additional embrittlement caused by the hardening effects of finer microstructure constituted by a significant amount of hydrogen remaining in solid solution within the Zr matrix and submicrometric hydrides, as observed in [41]. Furthermore, according to Bai [38], the materials tested at a faster strain rate exhibit lower ductility for a given set of hydrogen content and testing temperature, potentially resulting from the material viscosity. Our study's tensile tests were performed at a strain rate of 10^{-1} s^{-1}, which is much greater than those applied in other studies, commonly in the order of 10^{-4}-10^{-3} s^{-1} [12,31,37,38].

As shown in Fig. **10**, the DBT temperatures determined from our results in the case of materials only charged with oxygen are consistent with the results reported by Sawatzky [39] and Garde *et al*. [40]. Nonetheless, these DBT temperatures are higher by several tens of °C than those obtained by Stern *et al*. [6]. This difference would be explained by the difference in microstructure resulting from different cooling rates. Indeed, the samples tested by Stern *et al*. [6] were cooled at a faster rate (direct water-quenching), leading to a more brittle, finer, and more chemically homogeneous microstructure. In contrast, as illustrated in [26] and already discussed more in-depth in [24], in our case,

significant oxygen/hydrogen partitioning has occurred upon cooling at a few °C/s before the tensile tests, probably inducing localized “softer” zones within the tested (prior-)β_{Zr} structure.

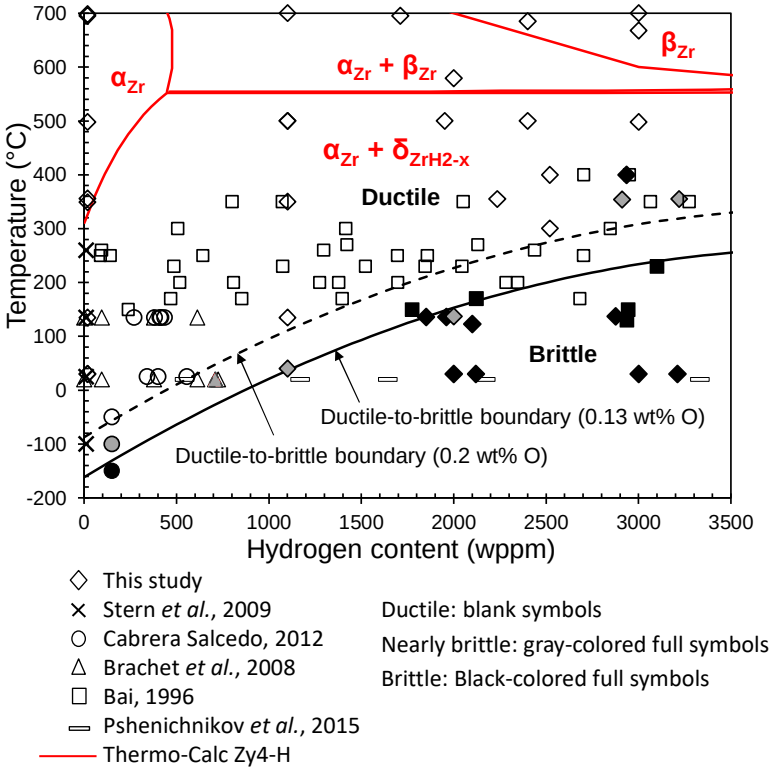

Fig. 9. DBT of the prior-β_{Zr} material as a function of temperature and hydrogen contents; data from our study and the literature [6,12,13,37,38]; pseudobinary Zircaloy-4-hydrogen phase diagram at equilibrium obtained by Thermo-Calc associated with the Zircobase database; DBT boundaries calculated by Eq. (2) for oxygen contents of 0.13 wt% (content for the data from the literature) and 0.2 wt% (content for the results from this study).

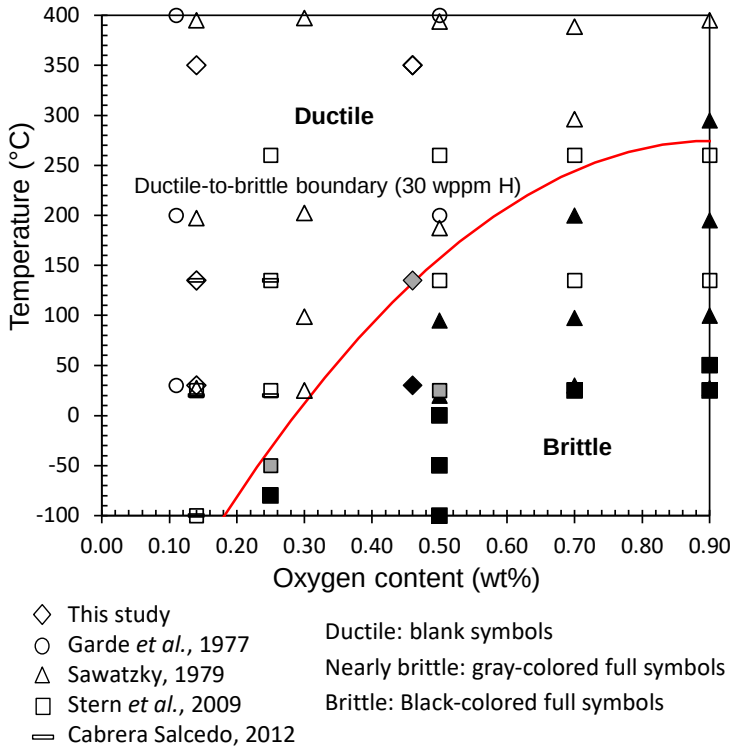

Fig. 10. DBT of the prior-β_{Zr} material as a function of temperature and oxygen content; data from our study and the literature [6,12,39,40]; DBT boundary calculated by Eq. (2) established in this study for 30 wppm of hydrogen.

Finally, Fig. **11** shows the macroscopic failure modes determined from our results as a function of temperature, hydrogen content and oxygen content. The macroscopic DBT temperatures are listed in Table **1**. It appears that hydrogen and oxygen have an additive effect (without strong coupling) on the DBT temperature that can reach about 580°C for the material containing about 2000 wppm hydrogen and 0.9 wt% oxygen. However, it should be recalled that the DBT temperatures discussed here refer to the macroscopic failure mode. As already reported in [11] and [37], ductile regions can be observed locally even when the behavior is macroscopically brittle. The discussion on the failure mechanisms at the microscale is out of the scope of this paper. More information can be found in [26]. However, it can be mentioned that this failure mode mixing brittle and ductile fracture at the microscale is mainly related to microchemical heterogeneities (oxygen and hydrogen in particular) due to partitioning during the β_{Zr}-to-α_{Zr} phase transformation upon cooling [24]. The distribution of oxygen and hydrogen, the fraction of hydrogen precipitated in the form of hydrides (or remaining in solid solution in the Zr matrix), the nature of hydrides and their proportion strongly depend on the cooling scenario and the average oxygen and hydrogen contents [26,41].

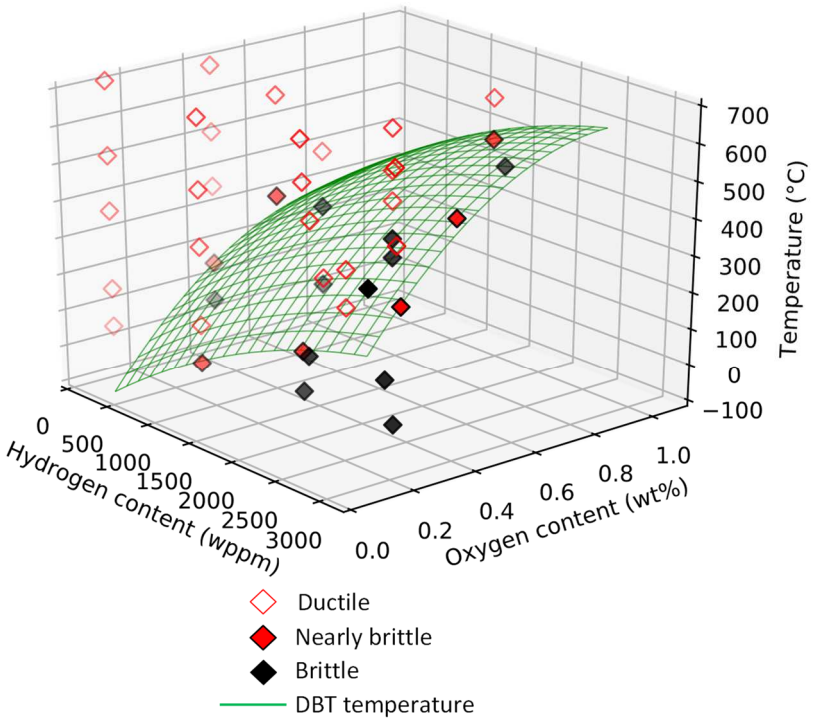

Fig. 11. Macroscopic DBT as a function of temperature, hydrogen content, and oxygen content for the prior-β_{Zr} material; DBT boundary calculated by Eq. (2).

Table 1. Macroscopic DBT temperatures of the (prior-)β_{Zr} material as a function of hydrogen and oxygen contents.

Hydrogen content (wppm)	Oxygen content (wt%)	DBT temperature (°C)
3	0.13	< 20
30	0.46	~ 135
1100-1200	0.13-0.15	~ 30
950	0.42-0.57	~ 400
1700-2400	0.17-0.24	~ 135
2200	0.44	400-500
2100	0.80-0.84	~ 580
2900-3200	0.19-0.22	350-400
2800	0.47	~ 500

3.4 Yield stress, ultimate tensile strength and uniform elongation

Fig. **12** and Fig. **13** show the evolutions of the YS and those of UTS as a function of temperature for several couples of hydrogen and oxygen contents. It is important to note that thin oxide and α_{Zr}(O) layers of only a few microns, formed by air oxidation at HT during the tensile tests, may have a slight effect on the material's global mechanical response, especially at the beginning of plasticity. However, considering their slight thicknesses, it is estimated that these layers result in a variation of only 5% in the stress levels. As shown in Fig. **12** and Fig. **13**, the YS and UTS increase continuously as the temperature decreases between 700 and 30°C in the case of ductile materials, regardless of hydrogen and oxygen contents.

Additionally, for a given oxygen content and at a given temperature below 500°C, the YS and UTS increase considerably in the presence of hydrogen up to 3000 wppm. The hardening effect of hydrogen in this temperature range would be related to the contribution of zirconium hydrides that extensively precipitate via a eutectoid transition taking place at around 500-550°C [41]. Besides, it may result from a significant amount of hydrogen potentially remaining in solid solution within the Zr matrix, as reported in [41]. However, the hydrogen-related effect appears not to significantly depend on the oxygen content. At 500°C, it is found that the YS and UTS increase slightly with increasing the hydrogen content up to 2000 wppm, then decrease slightly for higher hydrogen contents.

At temperatures above 500°C, *i.e.* 700°C, whatever the oxygen contents, both the YS and UTS tend to decrease slightly as the hydrogen content increases. This is consistent with the observations reported in [11] for the materials only charged with hydrogen. The softening effect of hydrogen at temperatures above 500°C can be explained by an increase in the β_{Zr} phase fraction at a given temperature above the eutectoid transition (in the two-phase domain, $\alpha_{Zr} + \beta_{Zr}$) with increasing the hydrogen content. Additionally, the β_{Zr} phase is known to have a lower mechanical strength at HT as compared to the α_{Zr} phase (prior-β_{Zr}). Furthermore, it is possible that interstitial hydrogen atoms in solid solution have the effect of weakening the atomic binding energy of zirconium [42] or of increasing the mobility of dislocations [43].

The oxygen-related strengthening effect for ductile materials can be clearly observed in Fig. **12** and Fig. **13**. However, it is found that this strengthening seems to be independent of or little dependent on the testing temperature. This is consistent with the results obtained by Sawatzky [39] on Zircaloy-4 samples only charged with oxygen. Additionally, the hardening effect of oxygen appears to be more significant for the non-hydrided samples as compared to the pre-hydrided ones. In the absence of hydrogen, the UTS values obtained in our study are higher than those reported by Stern *et al.* [6] and Sawatzky [39]. This difference would be related to material viscoplasticity. Indeed, the strain rate applied in our study is 300 times greater than those applied by Stern *et al.* and Sawatzky, in the order of 10^{-4} s^{-1}. The higher UTS values measured in our case could also be explained by a slower cooling from the β_{Zr} phase domain (about 1-10°C/s). Indeed, such a cooling promotes microstructure heterogeneities with larger oxygen-enriched α_{Zr} laths caused by the partitioning of oxygen during on-cooling phase transformation, which may give additional strengthening as a result of the intrinsic effect of oxygen in the case of ductile materials at HT [6].

Below the macroscopic DBT temperature, depending on the hydrogen and oxygen contents, it can be seen in Fig. **13** that the UTS, corresponding to the failure stress in the case of brittle fracture, decreases rapidly as the temperature decreases. It is only 128 MPa in the most brittle case tested, *i.e.* 2100 wppm hydrogen, 0.44 wt% oxygen, and 350°C. Besides, Fig. **13** clearly shows the embrittlement effects of hydrogen and oxygen. Precisely, below the DBT temperature, the failure stress is diminished as the hydrogen content increases for a given oxygen content, or as the oxygen content increases for a given hydrogen content, with no significant effect of temperature. Also, it seems that there is no significant coupling between the effects of hydrogen and oxygen. It is found that for a similar oxygen content and at a given temperature below

the DBT temperature, the failure stress obtained in our work is lower than that measured by Sawatzky [39]. Again, this may be due to the slower cooling applied in our work, promoting the formation of larger oxygen-enriched α_{Zr} laths, more brittle in the case of macroscopic brittle failure.

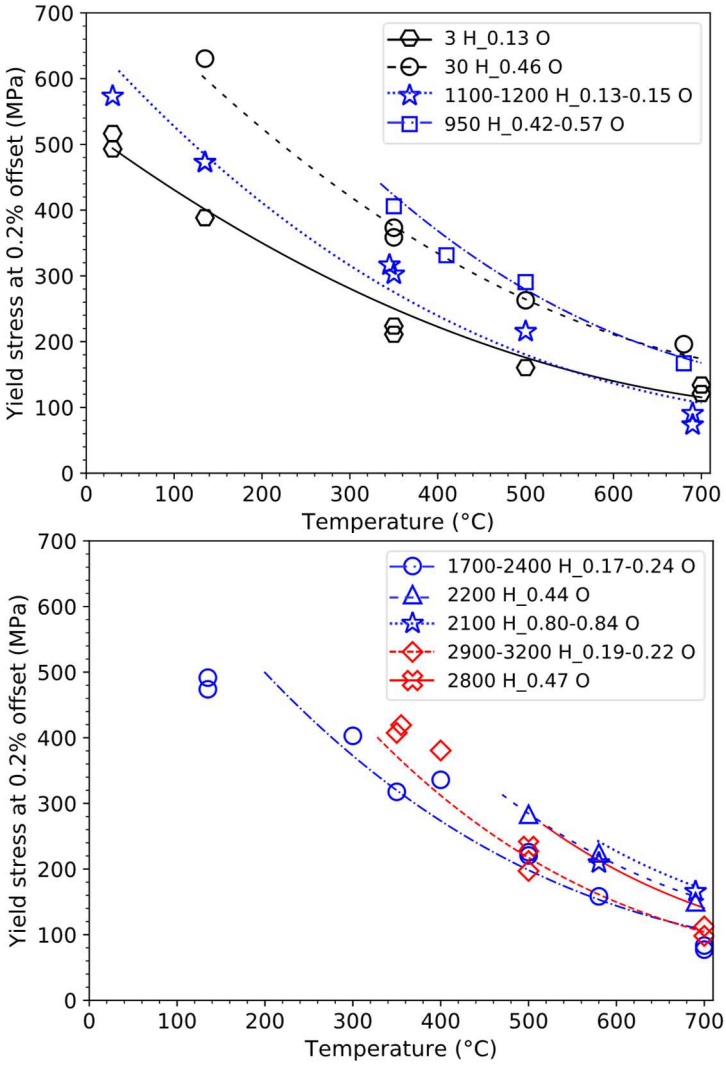

Fig. 12**.** Temperature dependence of the YS of the (prior-)β_{Zr} material charged at different hydrogen and oxygen contents; data on materials only charged with 1700-3200 wppm hydrogen are from [11]: experimental results (symbols) and predictions of the model presented in Section 4.4 (lines).

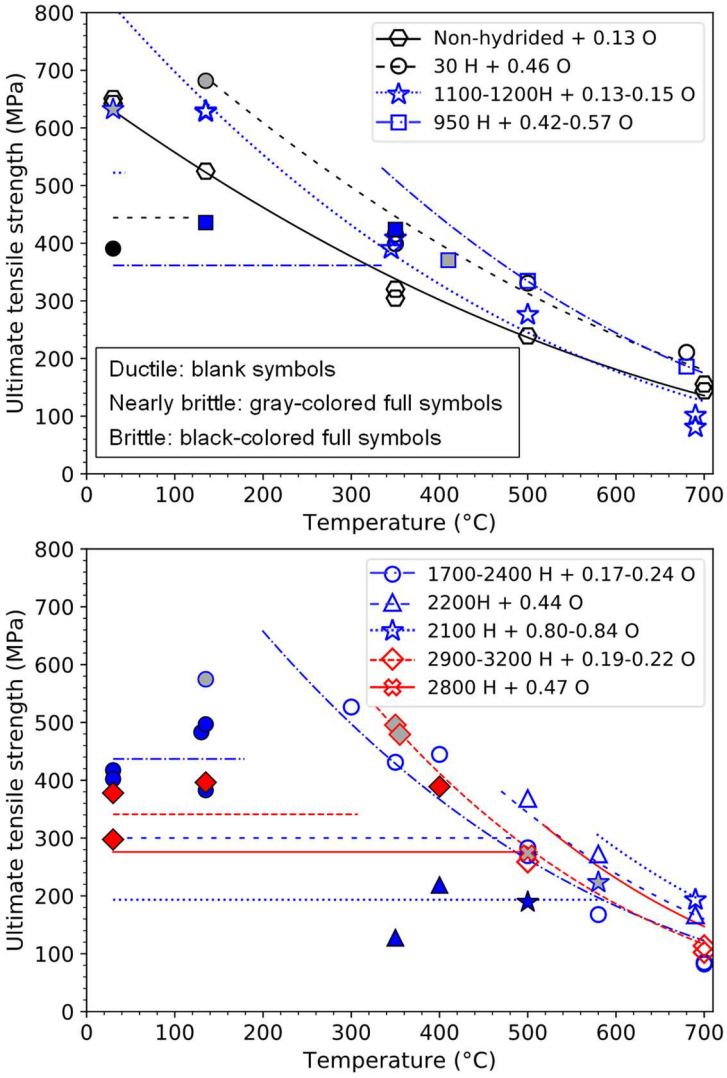

Fig. 13. Temperature dependence of the UTS of the (prior-)β_{Zr} material charged at different hydrogen and oxygen contents; data on materials only charged with 1700-3200 wppm hydrogen are from [11]: experimental results (symbols) and predictions of the model presented in Section 4.4 (lines).

Fig. **14** illustrates the influence of hydrogen and oxygen on the UE as a function of temperature. The UE tends to increase monotonically as the temperature decreases between 700 and 500°C, then decreases continuously for temperatures below, regardless of hydrogen and oxygen contents. These tendencies are consistent with those observed by Garde *et al.* [40] for Zircaloy-4 charged with about 0.5 wt% oxygen. At 700°C, the UE is significantly higher in the case of non-hydrided materials as compared to the materials charged with hydrogen. In the case of the hydrided materials, necking occurs very soon at the beginning of macroscopic plasticity for a very low plastic strain level. This rapid plastic strain localization in the presence of high hydrogen contents would be related to a larger fraction of the β_{Zr} phase and a higher amount of hydrogen in solid solution as compared to a non-hydrided material, resulting in a softening at this temperature. Besides, it seems that at 700°C, there is no obvious influence of oxygen on the UE for both non-hydrided and hydrided materials. This is in good agreement with the observations made by Garde *et al.* [40], who reported a nearly constant UE at 750°C for Zircaloy-4 charged at different oxygen contents up to about 0.9 wt%.

At a given temperature below 500°C, the UE decreases continuously as the hydrogen and oxygen contents increase due to the hardening and embrittlement effects of these two elements at these temperatures. This is consistent with the observations reported in the literature for samples only charged with either hydrogen or oxygen [6,11,40].

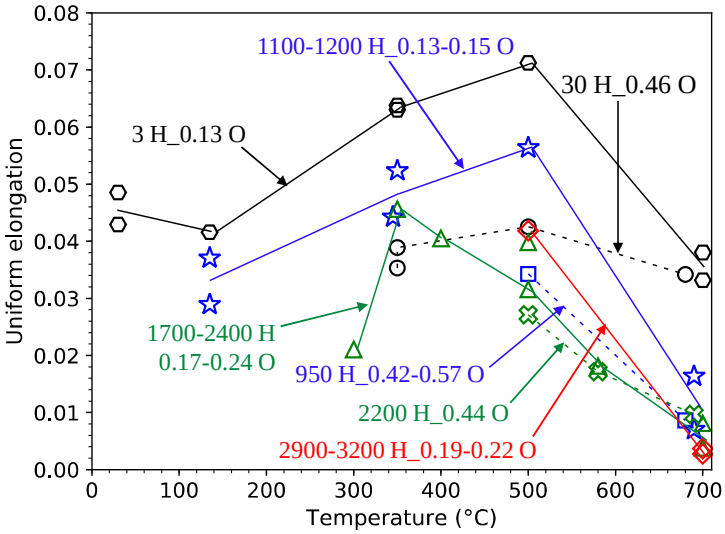

Fig. 14. Temperature dependence of the UE of the (prior-)β_{Zr} material charged at different hydrogen and oxygen contents; data on materials only charged with 1700-3200 wppm hydrogen are from [11].

4 Modeling

Based on the experimental data presented in the previous section, relationships are proposed to describe the uniaxial mechanical behavior of the material as a function of temperature and oxygen and hydrogen contents. It should be emphasized that these relationships are empirical/phenomenological, with no physical ingredients. For example, they do not explicitly take into account the evolution of the phases in the material. Therefore, there is no guarantee that they are relevant outside the strain rate, temperature, hydrogen content, and oxygen content ranges in which they have been established, *i.e.* strain rate of about 0.1 s^{-1}, temperatures between 30 and 700°C, hydrogen contents between a few wppm and 3200 wppm, and oxygen contents varying from 0.13 to 0.9 wt%. Furthermore, these relationships have been determined for materials cooled at a few °C/s to a few tenths of °C/s from the β_{Zr} domain. Thus, their application to materials subjected to very different cooling rates, *e.g.* direct water-quenching from the β_{Zr} domain, should be done with caution.

4.1 Elasticity

Elasticity is described by Hooke's law: $\sigma = E\varepsilon_e$, where σ is the Cauchy stress, ε_e is the logarithmic elastic strain. No significant effect of hydrogen and oxygen on E was observed. The following correlation is proposed to relate E (in GPa) to temperature T (in °C):

$$E = -0.07T + 91 \quad (1)$$

As shown in Fig. **6**, this relationship is capable of predicting reasonably well the experimental Young's moduli, with an uncertainty of ±10 GPa.

4.2 Ductile-to-brittle transition

On the basis of the experimental data obtained, the following correlation is proposed to describe the macroscopic DBT temperature as a function of hydrogen and oxygen contents by considering an additive effect of these two elements (no coupling):

$$T_c = -317.5 + (2100C_H - 2500C_H^2) + (1293.7C_O - 714.1C_O^2) \quad (2)$$

where C_H and C_O are the hydrogen content (in wt%) and the oxygen content (in wt%), respectively. T_c is the macroscopic DBT temperature in °C. For a given couple of hydrogen and oxygen contents, the material is considered as ductile when the testing temperature is higher than the critical temperature T_c. The boundary described by Eq. (2) is shown in Fig. **9**, Fig. **10**, and Fig. **11**, together with experimental data. It appears that this relationship describes satisfactorily well the DBT of the material charged either with hydrogen or oxygen, but also with both hydrogen and oxygen.

4.3 Brittle case: failure stress

In the case of brittle materials, *i.e.* at testing temperatures below the macroscopic DBT temperature T_c (Eq. (2)) for a given couple of hydrogen and oxygen contents, the evolution of the ultimate tensile stress UTS_b (in MPa), which corresponds to the failure stress, can be described by the following correlation:

$$UTS_b = 684\,(1 - 1.329C_H)(1 - 0.76C_O) \quad (3)$$

where C_H and C_O are expressed in wt%. This relationship takes into account the isolated effects of hydrogen and oxygen, as well as a slight coupling between the effects of these elements. As shown in Fig. **13**, the correlation estimates reasonably well, in the majority of cases, the failure stress of the brittle materials, with an uncertainty of a few tens of MPa, in particular at low temperatures, *i.e.* below 135°C, which is the saturation temperature during reflood in the LOCA scenario.

4.4 Ductile case: plastic flow

In the case of materials that exhibit a macroscopic ductile or nearly-brittle failure, *i.e.* when the testing temperature is higher than the macroscopic DBT temperature T_c, it can be interesting to have, as a first approach, simple relationships to determine the values of the YS and ultimate tensile strength UTS_d. The following relationships are proposed to describe the values of YS (in MPa) and UTS_d (in MPa) as a function of T (in °C) and C_H (in wt%), and C_O (in wt%), with a deviation smaller than 10% when compared to experimental values:

$$YS = (370.3 - 0.686T + 3.926\cdot10^{-4}T^2)(1 + 2.607(1 - \frac{T}{551})C_H)(1 + 3.318C_O - 1.997C_O^2) \quad (4)$$

$$UTS_d = (563.2 - 0.928T + 4.144\cdot10^{-4}T^2)(1 + 2.901(1 - \frac{T}{567.5})C_H)(1 + 1.290C_O - 0.245C_O^2) \quad (5)$$

As a second approach, it is even more interesting to have a model describing the plastic flow. For this purpose, the total strain is divided into a sum of elastic, ε_e, and plastic, ε_p, parts. The effect of viscosity is not taken into account since the tests were performed at a single strain rate of 10^{-1} s^{-1}. The elasticity is described by Hooke's law with the temperature-dependent elastic modulus given by Eq. (1). Once the initial yield stress σ_y is reached, the following isotropic and non-linear strain-hardening law is proposed to describe the evolution of the Cauchy stress σ as a function of the accumulated logarithmic plastic strain p:

$$\sigma(p) = \sigma_y + Hp + Q(1 - \exp(-Dp)) \quad (6)$$

In the case of monotonic tensile loading, $p = \varepsilon_p$. σ_y, H, Q, and D are material parameters. They were identified from the experimental stress-plastic strain data for plastic strain levels higher than 0.0005 to the onset of necking when it exists. Considering that plastic strain is isotropic and associated with no volume change, the logarithmic plastic strain and the Cauchy stress were determined from engineering plastic strain ε_{peng} and engineering stress σ_{eng} using the following relationships: $\varepsilon_p = \ln(1 + \varepsilon_{peng})$ and $\sigma = \sigma_{eng}(1 + \varepsilon_{peng})$.

First, the parameters of Eq. (6) were determined independently for each test, *i.e.* for a given set of temperature, hydrogen content, and oxygen content. Then, based on the results obtained, the following correlations were developed to describe the evolution of σ_y (in MPa), H (in MPa), Q (in MPa), and D (dimensionless) as a function of T (in °C), C_H (in wt%), and C_O (in wt%):

$$\sigma_y = (343.6 - 0.592T + 3.008\cdot10^{-4}T^2)(1 + 3.368(1 - \frac{T}{531.1})C_H)(1 + 2.827C_O - 1.563C_O^2) \quad (7)$$

$$H = (1800.7 - 4.033T + 2.647\cdot10^{-3}T^2)(1 + 4.722(1 - \frac{T}{811.6})C_H)(1 - 0.259C_O + 3.373C_O^2) \quad (8)$$

$$Q = (135 - 0.248T + 1.033\cdot10^{-4}T^2)(1 + 4.074C_H)(1 + 0.538C_O) \quad (9)$$

$$D = (241.6 - 1.254T + 1.911\cdot10^{-3}T^2)(1 + 1.038C_H)(1 - 0.145C_O - 0.593C_O^2) \quad (10)$$

These relationships include slight coupling between the effects of hydrogen and oxygen. As illustrated in Fig. **15**, the model reproduces reasonably well the evolution of the plastic flow stress and the effects of temperature and hydrogen and oxygen contents. As shown in Fig. 12 and Fig. **13**, it is able to predict the values of YS and UTS with an uncertainty lower than 10% (except the material containing about 3000 wppm hydrogen tested at 500°C for which the deviation reaches 15-20%).

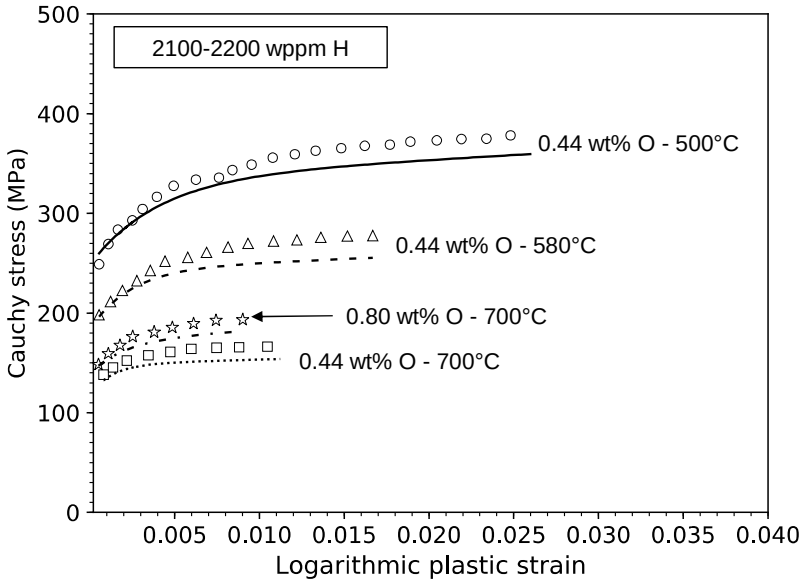

Fig. 15. Examples of stress-plastic strain curves, up to the experimental UE: experimental (symbols) and calculated (lines) for the (prior-)β_{Zr} material containing 2100-2200 wppm hydrogen and 0.44 or 0.8 wt% oxygen, tested at 500, 580, or 700°C.

5 Comparison to results obtained on claddings oxidized at HT

The relationships presented above describing the mechanical behavior of the (prior-)β_{Zr} material as a function of temperature and hydrogen and oxygen contents have been established on the basis of results of tensile tests performed with a strain rate of 0.1 s^{-1} on model materials. These materials were cooled at 5-6°C/s down to 700°C then at ~1-2°C/s from 700°C to 500°C, and finally at less than 1°C/s for lower temperatures. In this Section, the predictions of these relationships are compared to data from the literature obtained at RT on claddings oxidized at HT after pre-hydriding [8] or during semi-integral LOCA tests with secondary hydriding [7].

Desquines *et al.* [8] performed tensile tests at RT on Zircaloy-4 tube samples pre-hydrided up to 3500 wppm, oxidized under steam at 1200°C, then directly quenched into RT water. They reported global failure stress values calculated by dividing the failure load by the cladding's whole thickness, including the oxide and α_{Zr}(O) layers. These external layers exhibit more brittle behavior at low temperature than the underlying prior-β_{Zr} layer [24]. In claddings oxidized at HT, cracks are often observed in the α_{Zr}(O) layer after quenching (without additional mechanical loading) [25, 35]. These cracks are assumed to result from the internal stresses generated during cooling [44]. It is expected that cracks propagate in the oxide layer at the beginning of the tensile test performed after quenching [45]. Thus, it is assumed that the oxide and α_{Zr}(O) layers crack for a loading level significantly lower than the load leading to sample failure, so the load is only sustained by the prior-β_{Zr} layer. Hence, the failure stress values reported in [8] have been normalized to the section of the prior-β_{Zr} layer in the corresponding sample, which was evaluated from the total cladding thickness and the thicknesses of the oxide and the α_{Zr}(O) layers measured after oxidation. The comparison of our results to the data from [8] is only made for samples oxidized at 1200°C with an equivalent cladding reacted (ECR, *i.e.* total thickness of cladding metal that would be

converted into oxide, assuming that all the oxygen absorbed is reacted with the cladding to form stoichiometric ZrO_2) value of about 17% calculated using the Baker-Just equation [46]. For such oxidation conditions, the β_{Zr} layer's thickness remains significant and the oxygen solubility in this phase is nearly reached (without $\alpha_{Zr}(O)$ penetrations) in the presence of a large amount of hydrogen. Samples containing hydrogen contents between approximately 80 and 3000 wppm were considered. The prior-β_{Zr} layer in these samples is expected to be brittle (or nearly brittle) at RT, so Eq. (3) is used to predict the failure stresses. The hydrogen content in the metallic part is given in [8]. The oxygen content in the prior-β_{Zr} layer is not provided in [8]. During HT steam oxidation, a significant amount of oxygen diffuses from the oxide layer into the β_{Zr} layer. In the absence of hydrogen, the oxygen solubility in this phase at 1200°C is slightly above 0.4 wt%. The experimental failure stress values from [8] normalized to the prior-β_{Zr} section were compared to those calculated by Eq. (3) for 30°C with the hydrogen contents reported in [8] and 0.4 wt% oxygen. The results shown in Fig. **16** indicate that the calculated failure stresses are considerably higher than the experimental ones. Indeed, in the presence of hydrogen, the amount of oxygen diffusing into the β_{Zr} layer at HT is increased. The following relationship established by Brachet *et al*. [19] is used to estimate the oxygen content C_O (in wt%) in the prior-β_{Zr} layer of the samples tested in [8] from the hydrogen content C_H (in wppm):

$$C_O = 2 \cdot 10^{-4} C_H + 0.4395 \quad (11)$$

This relationship was established with hydrogen contents ranging from approximately 400 to 4000 wppm (and thus for oxygen contents between about 0.4 and 1.2 wt%), on the basis of measurements performed on samples steam oxidized for ~160s at 1200°C, corresponding to a Baker-Just ECR value close to 17% for two-sided HT oxidation. Fig. **16** shows the results obtained using the oxygen contents deduced from Eq. (11). The predictions are much closer to the experimental data when the additional oxygen content resulting from hydrogen's thermodynamic effect is taken into account. A deviation of a few tens of MPa is observed between the experimental and calculated failure stress values. This difference could be related to the internal stresses in the oxidized cladding resulting from cooling [44], which have not been taken into account. Besides, it could be due to the microstructure of the prior-β_{Zr} materials tested in this study as a result of the cooling rate applied [41]. However, despite these deviations, the trends are fully consistent. This shows that Eq. (3), established from results obtained on model materials, is able to describe, at least semi-quantitatively, the behavior of the prior-β_{Zr} layer, in the case of brittle failure, in claddings oxidized at HT, including the effects of hydrogen and oxygen.

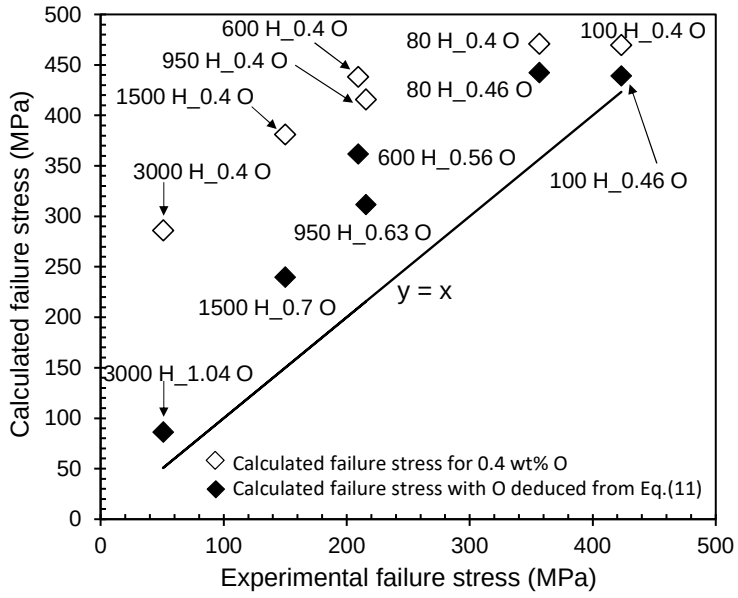

Fig. 16**.** Comparison of the experimental failure stress values (normalized to the prior-β_{Zr} section, reported in [8**]** for tensile tests performed at RT on Zircaloy-4 cladding samples pre-hydrided at several contents between 80 and 3000 wppm, oxidized under steam at 1200°C with a Baker-Just ECR of about 16-17%, then directly quenched into water at RT) and the failure stress values calculated by Eq. (3) (at RT) taking into account the hydrogen content in the prior-β_{Zr} material and 0.4 wt% oxygen or oxygen contents depending on the hydrogen contents deduced from Eq. (11); the corresponding hydrogen content (in wppm) and oxygen content (in wt%) are specified.

In [7], Thieurmel *et al.* presented results of semi-integral LOCA tests consisting of ballooning-burst, steam oxidation at 1200°C, cooling at 5-15°C/s down to 700°C followed by reflooding with RT water. Axial loads of 250, 540, and 750 N were applied during reflooding. As shown in Fig. **17**, they determined a local fracture/no-fracture threshold for the case of out-of-burst brittle failure, *i.e.* in the secondary hydrided region, during water-quenching from 700°C associated with additional tensile loading. They considered that the load is entirely sustained by the prior-β_{Zr} layer, so the failure stress was determined by reporting the applied load at failure to the cross-section of this layer. Besides, it was assumed that all the hydrogen is concentrated in the prior-β_{Zr} layer. So, the hydrogen content in this layer was determined from the mean hydrogen content measured at the failure location and its volume fraction. Then, Thieurmel *et al.* [7] proposed an equation, illustrated in Fig. **17**, that relates the failure stress of the prior-β_{Zr} layer to its hydrogen content. Fig. **17** shows the evolution of the failure stress determined from Eq. (3) for the prior-β_{Zr} material in the case of brittle failure at RT as a function of the hydrogen content, for 0.4 wt% oxygen. It can be seen that the failure stresses predicted for 0.4 wt% oxygen are significantly higher than those estimated by Thieurmel *et al*. [7]. Indeed, the oxygen content in the (prior-)β_{Zr} layer, which was not specified in [7], is expected to be higher than 0.4 wt% in the presence of high hydrogen contents, as discussed earlier. As shown in Fig. **17**, by considering the effect of additional oxygen in the (prior-)β_{Zr} phase using the correlations given in Eq. (11), the failure stress values calculated with Eq. (3) decreases considerably and become fully consistent with the experimental data reported by Thieurmel *et al.* [7]. This result confirms the importance of taking into account the additive effects of hydrogen and oxygen contents and the ability of the relationship developed to predict the failure stress

of the prior-β_{Zr} layer in the secondary hydrided regions of claddings having experienced a LOCA transient.

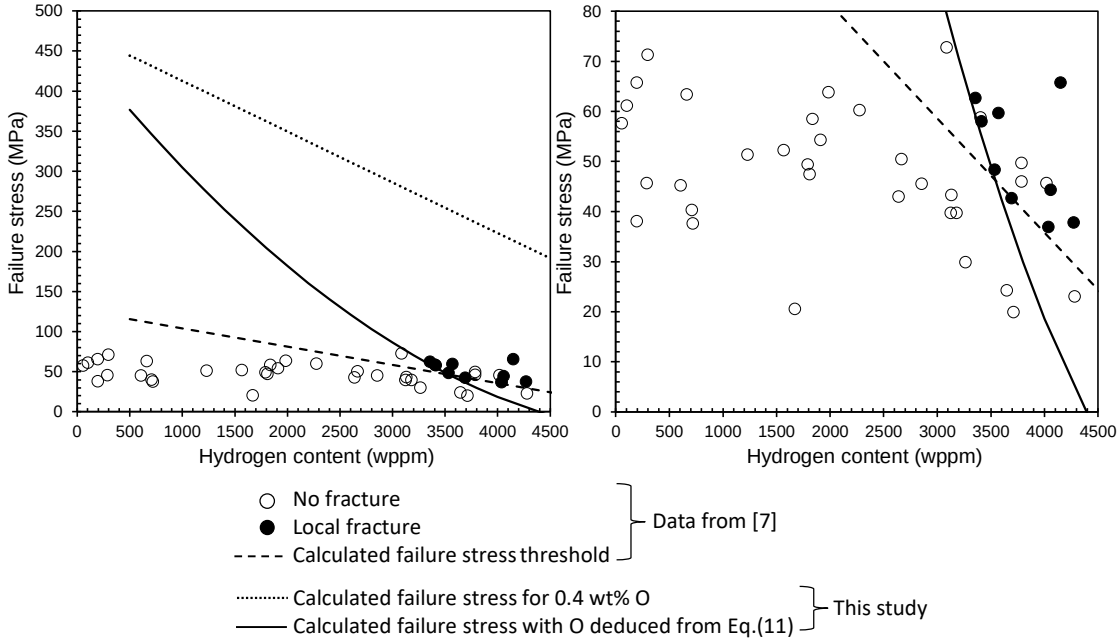

Fig. 17. Evolution of the failure stresses of the prior-β_{Zr} material as a function of its hydrogen content: values determined from semi-integral LOCA tests having led to out-of-burst failure during quenching from 700°C after oxidation at 1200°C associated with secondary hydriding [7] and associated values predicted with Eq. (3) (at RT) by taking into account the hydrogen content in the prior-β_{Zr} material and 0.4 wt% oxygen or oxygen contents depending on the hydrogen contents deduced from Eq. (11); magnification for failure stress values below 80 MPa.

6 Conclusions

This paper investigated the combined effects of temperature and of high hydrogen and oxygen contents on the macroscopic mechanical behavior of Zircaloy-4 upon cooling from the β_{Zr} phase temperature range. Model (prior-)β_{Zr} materials homogeneously charged at different hydrogen contents, up to about 3000 wppm, and oxygen contents, up to 0.9 wt%, were prepared from Zircaloy-4 cladding tubes such as those likely to be encountered in the LOCA-relevant secondary hydrided regions.

The mechanical behavior of the (prior-)β_{Zr} materials upon cooling from the β_{Zr} domain was characterized using uniaxial tensile tests performed at a strain rate of 10^{-1} s^{-1} and various temperatures between 700 and 30°C during cooling (at a cooling rate between a few °C/s to a few tenths of °C/s) from 1000-1200°C. Among the important findings are the following:

- The mechanical behavior of the (prior-)β_{Zr} material strongly depends on its hydrogen and oxygen contents and the loading temperature.
- The elastic modulus increases during cooling, with no significant effects of hydrogen and oxygen in the content ranges studied.
- For given hydrogen and oxygen contents, the material ductility decreases significantly as the temperature decreases. The macroscopic ductile-to-brittle

transition temperature increases continuously with increasing the hydrogen and oxygen contents, with an apparent additive effect of these two elements. It reaches about 580°C for the material containing about 2000 wppm hydrogen and 0.9 wt% oxygen.

- When the material is macroscopically ductile, the flow stress increases continuously with decreasing temperature, regardless of the hydrogen and oxygen contents. Oxygen has a strengthening effect, whatever the hydrogen content. This effect does not significantly depend on temperature in the range tested. Hydrogen has a softening effect above 500°C, mainly due to an increase in the proportion of the β_{Zr} phase and the hydrogen amount dissolved in this phase, regardless of oxygen content. Below 500°C, the hardening effect of hydrogen can be seen, resulting from the presence of both hydrides and/or hydrogen atoms potentially remaining in solid solution in the zirconium matrix at low temperatures.
- When the material is macroscopically brittle, *i.e.* at temperatures below the ductile-to-brittle transition temperature, the failure stress decreases as the hydrogen content and/or the oxygen content increase.
- Relationships are proposed to describe the macroscopic mechanical behavior of the material as a function of hydrogen and oxygen contents and temperature, *i.e.* ductile-to-brittle transition, elasticity, plasticity in case of ductile failure and failure stress in the case of brittle failure.
- The failure stresses predicted by the relationship proposed for the brittle case are consistent with some results reported in the literature. These results were obtained (i) by tensile tests performed on cladding tubes pre-charged with high hydrogen content, oxidized under steam at HT then water-quenched at room temperature, and (ii) by semi-integral LOCA tests in which the cladding, having experienced secondary hydriding during oxidation at HT, failed during quenching associated with additional loading. It emerges that taking into account the cumulative (additive) effects of hydrogen and oxygen is necessary to correctly predict the mechanical response during cooling of the cladding oxidized at HT with secondary hydriding. Thus, it is necessary to consider the higher oxygen content resulting from the thermodynamic effect of hydrogen on oxygen solubility and diffusivity.

The data and relationships obtained can be useful for finite element simulations to study the mechanical response, during and after cooling/quenching, of the claddings having undergone HT oxidation and secondary hydriding that show gradients of oxygen and hydrogen contents, such as those observed under LOCA conditions. Besides, these elements can be used to determine relevant testing conditions for semi-integral LOCA tests in the future.

The data have been obtained for a single strain rate. One perspective of this work would be to study the effect of strain rate. Furthermore, the materials tested were cooled at a moderate rate. Considering the cooling rate's effect on the microstructure of the (prior-)β_{Zr} material, it would be of interest to carry out the same characterizations on materials cooled at other rates, in particular faster ones. Indeed, the macroscopic mechanical behavior of the material is strongly related to the complex heterogeneous microstructure resulting from the phase transformations, microchemical partitioning of alloy elements,

in particular of hydrogen and oxygen, and hydride precipitation occurring during cooling. A first tensile test performed *in situ* under scanning electron microscope and fracture surface observations have shown that the deformation and the fracture of the material are heterogeneous at the microscale. The last perspective would be to improve understanding of the deformation and failure mechanisms at the local scale, as well as to relate the macroscopic mechanical behavior of the material to its microstructure.

Appendix A. Tabular data

Table A.1. Main mechanical properties of the (prior-)β_{Zr} material obtained from uniaxial tensile tests: T is the testing temperature estimated from the temperature measured on the specimen holder (see Section 2.2.3); C_H is the hydrogen content measured using HORIBA-EMGA 821 before the tensile tests; C_O is the oxygen content estimated from the weight gain after steam oxidation; E is the Young modulus; YS is the engineering stress at 0.2% of engineering plastic strain; UTS is the ultimate tensile strength; UE is the uniform elongation; and PSF is the plastic strain at failure; Z is the reduction of cross-section area at fracture.

T (°C)	C_H (wppm)	C_O (wt%)	E (GPa)	YS (MPa)	UTS (MPa)	UE (-)	PSF (-)	Z (-)	Macroscopic failure
30	17	0.13	99	517	651	0.043	0.063	0.12	Ductile
30	17	0.13	101	493	642	0.049	0.082	0.27	Ductile
135	17	0.13	79	388	525	0.042	0.085	0.27	Ductile
350	17	0.13	55	224	320	0.063	0.162	0.41	Ductile
350	17	0.13	59	211	305	0.064	0.142	0.43	Ductile
500	17	0.13	48	161	239	0.071	0.196	0.72	Ductile
700	17	0.13	38	121	144	0.033	0.298	0.99	Ductile
700	17	0.13	39	134	156	0.038	0.288	0.99	Ductile
30	30	0.46	90	-	391	0.000	0.000	0.04	Brittle
135	30	0.46	75	631	682	0.006	0.006	0.07	Nearly-brittle
350	30	0.46	67	373	416	0.035	0.086	0.07	Ductile
350	30	0.46	72	359	399	0.039	0.091	-	Ductile
500	30	0.46	55	263	331	0.043	0.126	0.22	Ductile
680	30	0.46	48	196	211	0.034	0.417		Ductile
30	1150	0.13	89	573	632	0.005	0.005	-0.04	Nearly-brittle
135	1150	0.13	70	473	629	0.037	0.042	-	Ductile
135	1150	0.13	74	473	628	0.029	0.031	0.13	Ductile
345	1150	0.13	60	317	391	0.044	0.128	0.18	Ductile
350	1150	0.13	63	303	409	0.052	0.152	-	Ductile
500	1150	0.13	51	216	276	0.056	0.186	-	Ductile
690	1150	0.13	42	91	101	0.016	0.271	-	Ductile
690	1150	0.13	40	73	81	0.007	0.241	-	Ductile
135	950	0.57	79	-	436	0.000	0.000	-	Brittle
350	950	0.57	62	406	424	0.003	0.003	0.06	Brittle
410	950	0.42	64	331	371	0.006	0.005	-	Nearly-brittle
500	950	0.57	46	290	335	0.034	0.118	0.39	Ductile
680	950	0.42	31	167	186	0.009	0.225	-	Ductile
30	930	0.81	74	-	126	0.000	0.000	-	Brittle
135	930	0.81	60	-	146	0.000	0.000	-	Brittle
350	860	0.82	50	-	298	0.000	0.000	-	Brittle
400	860	0.82	54	335	394	0.019	0.020	-	Ductile
500	930	0.81	33	290	331	0.026	0.073	-	Ductile
690	860	0.82	13	167	174	0.005	0.174	-	Ductile
30	2120	0.18	94	-	417	0.000	0.000	-0.03	Brittle
30	2000	0.21	82	-	402	0.000	0.000	0.09	Brittle
130	2100	0.2	67	-	483	0.002	0.002	0.09	Brittle
135	1850	0.18	63	-	383	0.000	0.000	-0.06	Brittle
135	2100	0.21	76	474	575	0.008	0.008	-0.04	Nearly-brittle
135	1960	0.2	70	492	497	0.002	0.002	0.12	Brittle
300	2520	0.2	54	403	527	0.021	0.021	0.10	Ductile
350	2000	0.21	55	318	431	0.046	0.102	0.47	Ductile

400	2520	0.2	46	336	445	0.040	0.098	0.53	Ductile
500	1950	0.19	36	221	270	0.032	0.154	0.74	Ductile
500	2400	0.18	41	226	283	0.040	0.167	0.68	Ductile
580	2000	0.21	37	158	168	0.018	0.246	0.99	Ductile
700	1710	0.19	25	77	82	0.008	0.296	0.99	Ductile
700	2400	0.19	26	83	85	0.004	0.357	0.99	Ductile
350	2200	0.44	79	-	128	0.000	0.000	-	Brittle
400	2200	0.44	64	-	219	0.000	0.000	-	Brittle
500	2200	0.44	47	283	368	0.027	0.037	0.10	Ductile
580	2200	0.44	48	225	272	0.017	0.138	0.21	Ductile
690	2200	0.44	32	150	167	0.010	0.176	0.29	Ductile
500	2100	0.84	49	-	189	0.001	0.001	0.11	Brittle
580	2100	0.8	47	209	223	0.003	0.004	0.08	Nearly-brittle
690	2100	0.8	35	166	193	0.010	0.081	0.21	Ductile
30	3210	0.185	99	-	298	0.000	0.000	0.10	Brittle
30	3000	0.21	97	-	378	0.000	0.000	0.25	Brittle
135	2875	0.22	68	-	396	0.000	0.000	0.08	Brittle
355	3220	0.22	58	419	479	0.007	0.007	0.11	Nearly-brittle
350	2910	0.21	56	407	496	0.010	0.010	-0.07	Nearly-brittle
400	2935	0.15	54	381	389	0.002	0.002	0.10	Brittle
500	3000	0.22	49	197	259	0.042	0.163	0.74	Ductile
700	3000	0.22	42	113	114	0.003	0.308	0.99	Ductile
700	3000	0.21	40	98	102	0.004	0.278	0.99	Ductile
500	2800	0.47	62	235	274	0.005	0.005	0.01	Nearly-brittle

Acknowledgments

The authors would like to thank P. Bossis from DES-DMN (CEA); P. Berger from LEEL (CEA); C. Cobac, G. Nony, and Q. Barrès from DES-SRMA (CEA); J.D. Bartout, R. Clement, J.C. Teissedre, S. Dang, and A. Meddour from MINES ParisTech; and EDF and Framatome, for their contributions to this work. This work was funded by the French Nuclear Institute in the framework of the GAINES project.

References

[1] G. Hache, H.M. Chung, The history of LOCA embrittlement criteria, Argonne Natl. Lab ANLCP-102703. (2001).

[2] M. Billone, Y. Yan, T. Burtseva, R. Daum, Cladding embrittlement during postulated loss-of-coolant accidents, Argonne Natl. Lab IL USA NUREGCR-696. (2008).

[3] F. Nagase, Behavior of LWR fuel during loss-of-coolant accidents, Compr. Nucl. Mater. 2. (2012) 595–608.

[4] J.C. Brachet, L. Portier, T. Forgeron, J. Hivroz, D. Hamon, T. Guilbert, T. Bredel, P. Yvon, J.P. Mardon, P. Jacques, Influence of hydrogen content on the alpha/beta phase transformation temperatures and on the thermal-mechanical behavior of Zy4, M4 (ZrSnFeV) and M5 (ZrNbO) alloys during the first phase of LOCA transient, Zircon. Nucl. Ind. Thirteen. Int. Symp. (2002) 673–701. https://doi.org/10.1520/STP11411S.

[5] O.T. Woo, K. Tangri, Transformation characteristics of rapidly heated and quenched zircaloy-4-oxygen alloys, J. Nucl. Mater. 79 (1979) 83–94. https://doi.org/10.1016/0022-3115(79)90435-5.

[6] A. Stern, J.-C. Brachet, V. Maillot, D. Hamon, F. Barcelo, S. Poissonnet, A. Pineau, J.-P. Mardon, A. Lesbros, Investigations of the Microstructure and Mechanical Properties of Prior-β Structure as a Function of the Oxygen Content in Two Zirconium Alloys, J. ASTM Int. 5 (2009) 71–118. https://doi.org/10.1520/JAI101119.

[7] R. Thieurmel, J. Besson, E. Pouillier, A. Parrot, A. Ambard, A.-F. Gourgues-Lorenzon, Contribution to the understanding of brittle fracture conditions of zirconium alloy fuel cladding tubes during LOCA transient, J. Nucl. Mater. 527 (2019) 151815. https://doi.org/10.1016/j.jnucmat.2019.151815.

[8] J. Desquines, D. Drouan, S. Guilbert, P. Lacote, Embrittlement of pre-hydrided Zircaloy-4 by steam oxidation under simulated LOCA transients, J. Nucl. Mater. 469 (2016) 20–31. https://doi.org/10.1016/j.jnucmat.2015.11.008.

[9] F. Nagase, T. Fuketa, Behavior of Pre-hydrided Zircaloy-4 Cladding under Simulated LOCA Conditions, J. Nucl. Sci. Technol. 42 (2005) 209–218.

[10] R. Chosson, A.F. Gourgues-Lorenzon, V. Vandenberghe, J.C. Brachet, J. Crépin, Creep flow and fracture behavior of the oxygen-enriched alpha phase in zirconium alloys, Scr. Mater. 117 (2016) 20–23.

[11] I. Turque, R. Chosson, M. Saux, J.-C. Brachet, V. Vandenberghe, J. Crépin, A.-F. Gourgues-Lorenzon, Mechanical Behavior at High Temperatures of Highly Oxygen- or Hydrogen-Enriched α and Prior-β Phases of Zirconium Alloys, Zircon. Nucl. Ind. 18th Int. Symp. ASTM STP 1597 R Comstock Motta Eds ASTM Int. West Conshohocken PA. (2018) 240–280. https://doi.org/10.1520/STP159720160063.

[12] A. Cabrera Salcedo, Modélisation du comportement mécanique “post-trempe”, après oxydation à haute température, des gaines de combustible des réacteurs à eau pressurisée, PhD Thesis Fr. MINES ParisTech Fr. (2012).
[13] J.C. Brachet, V. Vandenberghe-Maillot, L. Portier, D. Gilbon, A. Lesbros, N. Waeckel, J.P. Mardon, Hydrogen content, pre-oxidation and cooling scenario effects on postquench microstructure and mechanical properties of Zircaloy-4 and M5 alloys in LOCA conditions, J. ASTM Int. 5 (2008) 1–28. https://doi.org/10.1520/JAI101116.
[14] H.M. Chung, A.M. Garde, T.F. Kassner, Development of an Oxygen Embrittlement Criterion for Zircaloy Cladding Applicable to Loss-of-Coolant Accident Conditions in Light-Water Reactors, Zircon. Nucl. Ind. ASTM Int. ASTM STP681. (1979) 600–627. https://doi.org/10.1520/STP36703S.
[15] H. Uetsuka, T. Furuta, S. Kawasaki, Failure-Bearing Capability of Oxidized Zircaloy-4 Cladding under Simulated Loss-of -Coolant Condition, J. Nucl. Sci. Technol. 20 (1983) 941–950. http://dx.doi.org/10.1080/18811248.1983.9733491.
[16] Z. Hózer, I. Nagy, A. Vimi, M. Kunstár, P. Szabó, T. Novotny, E. Perez-Feró, Z. Kis, L. Szentmiklósi, M. Horváth, A. Csordás, E. Barsy, K. Kulacsy, M. Grosse, High-Temperature Secondary Hydriding Experiments with E110 and E110G Claddings, Zircon. Nucl. Ind. 18th Int. Symp. (2018). https://doi.org/10.1520/STP159720160031.
[17] J. Stuckert, M. Große, C. Rössger, M. Klimenkov, M. Steinbrück, M. Walter, QUENCH-LOCA program at KIT on secondary hydriding and results of the commissioning bundle test QUENCH-L0, Nucl. Eng. Des. 255 (2013) 185–201. https://doi.org/10.1016/j.nucengdes.2012.10.024.
[18] J. Stuckert, M. Grosse, M. Steinbrueck, M. Walter, A. Wensauer, Results of the QUENCH-LOCA experimental program at KIT, J. Nucl. Mater. 534 (2020) 152143. https://doi.org/10.1016/j.jnucmat.2020.152143.
[19] J.-C. Brachet, D. Hamon, M. Le Saux, V. Vandenberghe, C. Toffolon-Masclet, E. Rouesne, S. Urvoy, J.-L. Béchade, C. Raepsaet, J.-L. Lacour, G. Bayon, F. Ott, Study of secondary hydriding at high temperature in zirconium based nuclear fuel cladding tubes by coupling information from neutron radiography/tomography, electron probe micro analysis, micro elastic recoil detection analysis and laser induced breakdown spectroscopy microprobe, J. Nucl. Mater. 488 (2017) 267–286. https://doi.org/10.1016/j.jnucmat.2017.03.009.
[20] Y. Okada, M. Amaya, Effects of oxidation and secondary hydriding during simulated loss-of-coolant-accident tests on the bending strength of Zircaloy-4 fuel cladding tube, Ann. Nucl. Energy. 136 (2020) 107028. https://doi.org/10.1016/j.anucene.2019.107028.
[21] S. Guilbert-Banti, P. Lacote, G. Taraud, P. Berger, J. Desquines, C. Duriez, Influence of hydrogen on the oxygen solubility in Zircaloy-4, J. Nucl. Mater. 469 (2016) 228–236. https://doi.org/10.1016/j.jnucmat.2015.11.019.
[22] H.M. Chung, T.F. Kassner, Pseudobinary zircaloy-oxygen phase diagram, J. Nucl. Mater. 84 (1979) 327–339. https://doi.org/10.1016/0022-3115(79)90172-7.
[23] L. Portier, T. Bredel, J.C. Brachet, V. Maillot, J.-P. Mardon, A. Lesbros, Influence of Long Service Exposures on the Thermal-Mechanical Behavior of Zy-4 and M5^{TM} Alloys in LOCA Conditions, J. ASTM Int. 2 (2005) 1–24. https://doi.org/10.1520/JAI12468.

[24] J.C. Brachet, D. Hamon, J.L. Béchade, P. Forget, C. Toffolon-Masclet, C. Raepsaet, J.P. Mardon, B. Sebbari, Quantification of the chemical elements partitioning within pre-hydrided Zircaloy-4 after high temperature steam oxidation as a function of the final cooling scenario (LOCA conditions) and consequences on the (local) materials hardening, Proceeding IAEA Tech. Meet. Fuel Behav. Model. Sev. Transient LOCA Cond. Jpn. (2013) 253–265.
[25] B. Mazères, C. Desgranges, C. Toffolon-Masclet, D. Monceau, Contribution to Modeling of Hydrogen Effect on Oxygen Diffusion in Zy-4 Alloy During High Temperature Steam Oxidation, Oxid. Met. 79 (2013) 121–133. https://doi.org/10.1007/s11085-012-9335-1.
[26] T. Le Hong, Effets de l'oxygène et de l'hydrogène sur la microstructure et le comportement mécanique d'alliages de zirconium après incursion à haute température, PhD Thesis Fr. MINES ParisTech Fr. (2020). https://pastel.archives-ouvertes.fr/tel-02887252.
[27] M. Steinbrück, Hydrogen absorption by zirconium alloys at high temperatures, J. Nucl. Mater. 334 (2004) 58–64.
[28] V. Vandenberghe, J.C. Brachet, M. Le Saux, D. Gilbon, M. Billone, D. Hamon, J.P. Mardon, B. Hafidi, Influence of the Cooling Scenario on the Post-Quench Mechanical Properties of Pre-Hydrided Zircaloy-4 Fuel Claddings after high Temperature Steam Oxidation (LOCA Conditions), Proc. 2010 LWR Fuel PerformanceTopFuelWRFPM Orlando Fla. USA. (2010) 270–277.
[29] M. Le Saux, V. Vandenberghe, P. Crébier, J.C. Brachet, D. Gilbon, P. Jacques, A. Cabrera Salcedo, Influence of Steam Pressure on the High Temperature Oxidation and Post-Cooling Mechanical Properties of Zircaloy-4 and M5 Cladding (LOCA Conditions), Zircon. Nucl. Ind. 17th Int. Symp. STP 1543. (2014) 1002–1053. https://doi.org/10.1520/STP154320120196.
[30] M. Le Saux, J.-C. Brachet, V. Vandenberghe, A. Ambard, R. Chosson, Breakaway oxidation of zirconium alloys exposed to steam around 1000 °C, Corros. Sci. 176 (2020) 108936. https://doi.org/10.1016/j.corsci.2020.108936.
[31] A. Stern, Comportement métallurgique et mécanique des matériaux de gainage du combustible REP oxydés à haute température, PhD Thesis Fr. MINES ParisTech Fr. (2007).
[32] N. Dupin, I. Ansara, C. Servant, C. Toffolon, C. Lemaignan, J.C. Brachet, A thermodynamic database for zirconium alloys, J. Nucl. Mater. 275 (1999) 287–295. https://doi.org/10.1016/S0022-3115(99)00125-7.
[33] J.C. Brachet, S. Urvoy, E. Rouesne, G. Nony, M. Dumerval, M.L. Saux, F. Ott, A. Michau, F. Schuster, F. Maury, DLI-MOCVD CrxCy coating to prevent Zr-based cladding from inner oxidation and secondary hydriding upon LOCA conditions, J. Nucl. Mater. 550 (2021) 152953. https://doi.org/10.1016/j.jnucmat.2021.152953.
[34] P. Lafaye, C. Toffolon-Masclet, J.-C. Crivello, J.-M. Joubert, Experimental investigations and thermodynamic modelling of the Cr–Nb–Sn–Zr system, Calphad. 64 (2019) 43–54. https://doi.org/10.1016/j.calphad.2018.11.002.
[35] F. Nagase, T. Fuketa, Fracture Behavior of Irradiated Zircaloy-4 Cladding under Simulated LOCA Conditions, J. Nucl. Sci. Technol. 43 (2006) 1114–1119. https://doi.org/10.1080/18811248.2006.9711202.
[36] L.R. Bunnell, G.B. Mellinger, J.L. Bates, High-temperature properties of Zy-O alloys, EPRI NP-524 Res. Proj. 251-1. (1977).

[37] A. Pshenichnikov, J. Stuckert, M. Walter, Microstructure and mechanical properties of Zircaloy-4 cladding hydrogenated at temperatures typical for loss-of-coolant accident (LOCA) conditions, Nucl. Eng. Des. 283 (2015) 33–39. https://doi.org/10.1016/j.nucengdes.2014.06.022.
[38] J.B. Bai, Effect of Hydriding Temperature and Strain Rate on the Ductile-Brittle Transition in β Treated Zircaloy-4, J. Nucl. Sci. Technol. 33 (1996) 141–146. https://doi.org/10.1080/18811248.1996.9731876.
[39] A. Sawatzky, A Proposed Criterion for the Oxygen Embrittlement of Zircaloy-4 Fuel Cladding, Zircon. Nucl. Ind. ASTM STP681 J H Schemel T P Papazoglou Eds ASTM Int. Phila. PA. (1979) 479–496. https://doi.org/10.1520/STP36697S.
[40] A.M. Garde, H.M. Chung, T.F. Kassner, Uniaxial tensile properties of Zircaloy containing oxygen: summary report, ANL-77-30 Argonne Natl. Lab. (1977).
[41] T. Le Hong, I. Turque, J.-C. Brachet, J. Crépin, G. André, Q. Barres, R. Guillou, C. Toffolon-Masclet, J.-M. Joubert, M. Le Saux, Phase transformations during cooling from the βZr phase temperature domain in several hydrogen-enriched zirconium alloys studied by in situ and ex situ neutron diffraction, Acta Mater. 199 (2020) 453–468. https://doi.org/10.1016/j.actamat.2020.08.061.
[42] S. Yamanaka, D. Setoyama, H. Muta, M. Uno, M. Kuroda, K. Takeda, T. Matsuda, Characteristics of zirconium hydrogen solid solution, J. Alloys Compd. 372 (2004) 129–135. https://doi.org/10.1016/j.jallcom.2003.09.140.
[43] N. Rupa, Effet de l'hydrogène et des hydrures sur le comportement viscoplastique du zircaloy-4 recristallisé, PhD Thesis Fr. Univ. Technol. Compiègne Fr. (2000).
[44] M. Le Saux, T. Guilbert, J.C. Brachet, An approach to study oxidation-induced stresses in Zr alloys oxidized at high temperature, Corros. Sci. 140 (2018) 79–91.
[45] J. Desquines, D. Drouan, E. Torres, S. Guilbert, P. Lacote, An attempt for a unified description of mechanical testing on Zircaloy-4 cladding subjected to simulated LOCA transient, J. Nucl. Sci. Technol. 2 (2016).
[46] L.Jr. Baker, L.C. Just, Studies of Metal–Water Reactions at High Temperatures. III. Experimental and Theoretical Studies of the Zirconium–Water Reaction, Argonne Natl. Lab ANL Argonne IL USA ANL-6548. (1962).